Research Square

Preprints are preliminary reports that have not undergone peer review.
They should not be considered conclusive, used to inform clinical practice,
or referenced by the media as validated information.

Raw Sugarcane Bagasse Hydrochar Outperforms Carbon Nanotubes in Microbial Fuel Cell Power Generation

Abdul Azeez Olayiwola Sirajudeen
sirajudeen@uniten.edu.my
Universiti Tenaga Nasional
Kamil Kayode Katibi
Universiti Putra Malaysia
Mohamad Suffian Mohamad Annuar
University of Malaya
Shaliza Ibrahim
Universiti Tenaga Nasional
Muhammad Aliyu
Chulalongkorn University
Temitope Theophilus Dele-Afolabi
Universiti Teknologi MARA
Mohd Arif Dar
University of Malaya
Siti Rohana Majid
University of Malaya

Research Article

Keywords: Bioelectrochemical systems, waste valorization, hydrothermal carbonization, sustainable electrodes, biofilm-electrode interface

Posted Date: July 9th, 2026

DOI: https://doi.org/10.21203/rs.3.rs-8607469/v1

License: This work is licensed under a Creative Commons Attribution 4.0 International License.
Read Full License

Additional Declarations: No competing interests reported.

Version of Record: A version of this preprint was published at Biomass Conversion and Biorefinery on October 30th, 2026. See the published version at https://doi.org/10.1007/s13399-026-07326-0.

Raw Sugarcane Bagasse Hydrochar Outperforms Carbon Nanotubes in Microbial Fuel Cell Power Generation

Abdul Azeez Olayiwola Sirajudeen [1,2,*], Kamil Kayode Katibi [3], Mohamad Suffian Mohamad Annuar [4*], Shaliza Ibrahim [1,5], Muhammad Aliyu [6], Temitope Theophilus Dele-Afolabi [7], Mohd Arif Dar [8,9], Siti Rohana Majid [8]

[1] *Institute of Sustainable Energy, Universiti Tenaga Nasional, 43000 Kajang, Selangor, Malaysia*

[2] *Department of Biological Sciences, College of Natural and Applied Sciences, Crescent University, 110001 Abeokuta, Nigeria*

[3] *Department of Physics, Faculty of Science, University Putra Malaysia, 43400 Serdang, Selangor, Malaysia*

[4] *Institute of Biological Sciences, Faculty of Science, Universiti Malaya, 50603 Kuala Lumpur, Malaysia*

[5] *Institute of Ocean and Earth Sciences, Universiti Malaya, 50603 Kuala Lumpur, Malaysia*

[6] *Department of Chemical Technology, Faculty of Science, Chulalongkorn University, Bangkok 10330, Thailand*

[7] *School of Mechanical Engineering, College of Engineering, Universiti Teknologi MARA, 40450 Shah Alam, Selangor, Malaysia*

[8] *Centre for Ionics University Malaya, Department of Physics, Universiti Malaya, 50603 Kuala Lumpur, Malaysia*

[9] *Faculty of Allied Health Sciences, Chettinad Hospital and Research Institute, Chettinad Academy of Research and Education, Kelambakkam 603103 Tamil Nadu, India*

*Corresponding Authors:

Dr. Abdul Azeez O. Sirajudeen
Institute of Sustainable Energy
Universiti Tenaga Nasional
43000 Kajang, Selangor, Malaysia
e-mail: sirajudeen@uniten.edu.my

Professor Dr. M. Suffian M. Annuar
Institute of Biological Sciences
Faculty of Science, Universiti Malaya
50603 Kuala Lumpur, Malaysia
e-mail: suffian_annuar@um.edu.my
Tel: +60379677182
Fax: +60379674178

Abstract

The commercialization of microbial fuel cells (MFCs) is currently limited by the high cost of standard electrode materials like carbon nanotubes (CNTs). This study introduces a high-performance, low-cost alternative: sugarcane bagasse hydrochar. We evaluated raw (RSBH), phosphated (PSBH), and sulfonated (SSBH) hydrochars as symmetric electrodes against a commercial CNT control. While acid functionalization enhanced thermal stability and char yields, the unmodified hydrochar yielded the most striking electrochemical results. Ni-RSBH achieved a peak power density of 1008 mW/m^2, quadrupling the performance of the commercial Ni-CNT (235 mW/m^2). Post-operation analysis revealed that Ni-RSBH developed exceptional biofilm compatibility, with anodic capacitance surging to 51.03 F/g compared to just 3.01 F/g for Ni-CNT. Although the phosphated variant (Ni-PSBH) offered superior voltage stability (0.68–0.71 V), the raw hydrochar provided the optimal balance of conductivity and biological activity. These findings demonstrate that minimally processed agricultural waste can outperform engineered nanomaterials, presenting a scalable, circular-economy solution for bioelectrochemical systems.

Keywords: Bioelectrochemical systems, waste valorization, hydrothermal carbonization, sustainable electrodes, biofilm-electrode interface

1. Introduction

Global warming, predominantly driven by greenhouse gas emissions from fossil fuel combustion, represents one of the most pressing environmental challenges confronting contemporary society [1, 2]. Despite concerted scientific efforts to mitigate global temperature increases, empirical evidence demonstrates accelerated warming trends, necessitating urgent advancement of renewable energy technologies [3, 4]. Microbial fuel cells (MFCs) have emerged as a particularly promising renewable energy platform, offering the dual functionality of electricity generation

coupled with simultaneous wastewater treatment [5]. A conventional dual-chambered MFC comprises an anode and cathode compartment separated by an ion-selective membrane, wherein microorganisms oxidize wastewater at the anode while protons generated during oxidation traverse the membrane to the cathode for reduction reactions, thereby completing the redox cycle [6, 7].

Electrode modification with conducting materials has become a fundamental strategy for optimizing redox reactions in MFC systems [8]. Enhanced electron transfer at the anode and accelerated oxygen reduction at the cathode, achieved through electrode coating, have substantially improved overall power output [9, 10]. Although highly purified conductive nanomaterials such as carbon nanotubes, graphene, Fe_3O_4, carbon black, and platinum-on-carbon composites have demonstrated impressive power generation capabilities, their prohibitively high costs present significant barriers to large-scale implementation [11-14]. Consequently, recent investigations have focused on electrode modifiers derived from agricultural waste materials. Ahmad [15] synthesized graphene oxide electrodes from moringa biomass for MFC applications, reporting enhanced power density, elevated voltage output, and reduced internal resistance compared to unmodified controls, alongside remarkable heavy metal removal efficiencies of 75.10 % for lead and 65 % for mercury. Similarly, carbon-based electrode materials derived from durian shell waste have been developed for concurrent dye degradation and electricity generation, achieving power densities of 5,184 mW/m^3 and degradation efficiencies of 96.36 % [16].

Biochar, derived from diverse waste feedstocks including municipal sludge [17], kitchen waste, wood chips [18], pineapple peel, corn straw, and rice husk [19], represents a sustainable and increasingly utilized material for both energy storage and pollutant removal in MFC systems. However, hydrochar—a carbon-rich solid produced *via* hydrothermal carbonization of wet

biomass at moderate temperatures (180–250 °C) under autogenous pressure—offers distinct advantages [20, 21]. Unlike conventional carbonization methods requiring energy-intensive feedstock processing, hydrothermal carbonization processes wet biomass directly without preliminary desiccation, yielding up to 70 % mass recovery with reduced ash and heavy metal contamination and enhanced oxygenated functional group abundance [22, 23].

Sugarcane bagasse (SB), a significantly underutilized lignocellulosic byproduct of sugar and ethanol processing, represents an abundant and readily available agro-waste resource, with billions of tons generated globally annually [24]. SB demonstrates superior characteristics compared to alternative agro-waste biomasses for advanced carbon material synthesis, including its renewability, economical accessibility, and distinctive compositional profile comprising approximately 42–50 % cellulose, 20–30 % hemicellulose, and 15–25 % lignin [25, 26]. The inherent porosity, minimal ash content (less than 5 %), and favorable chemical composition for heteroatom doping confer additional advantages over competing agro-waste feedstocks [27, 28].

While hydrochars from various biomass sources have shown promise as low-cost electrode materials in bioelectrochemical systems, their performance is highly dependent on feedstock selection and surface chemistry. Sugarcane bagasse, despite its abundance and favorable lignocellulosic composition, remains underexplored as a hydrochar precursor for symmetric MFC electrodes. Furthermore, the comparative impact of chemical functionalization (phosphation vs. sulfonation) on the electrochemical performance and biofilm compatibility of the same hydrochar substrate has not been systematically evaluated against commercial benchmarks. This study addresses this specific gap by comprehensively investigating raw, phosphated, and sulfonated sugarcane bagasse hydrochars as symmetric electrodes, directly benchmarking their performance

against commercial carbon nanotubes across multiple electrochemical and operational parameters in long-term MFC operation. The functionalization of raw hydrochar was aimed to enhance porosity, surface area, and functional group density. Comprehensive structural, morphological, thermogravimetric, and electrochemical characterization were conducted prior to evaluation in dual-chambered MFC configurations.

2. Materials and Methods

2.1 Materials

Raw sugarcane bagasse was obtained from a local open market in Sri Serdang, Seri Kembangan, Selangor, Malaysia. Analytical-grade ethanol, methanol, sulfuric and phosphoric acid were procured from Sigma-Aldrich (USA). The Nafion 117 membrane was procured from Dupont (USA), while multiwalled carbon nanotubes (≥ 98 % carbon basis) and polytetrafluoroethylene (PTFE) binder were both sourced from Sigma-Aldrich (USA). All chemicals used in this study are of analytical grade and employed directly without further purification steps.

2.2 Preparation of Hydrochar from Sugarcane Bagasse

The preparation process began with the raw sugarcane bagasse being thoroughly washed with distilled water to eliminate dirt and debris. Once cleaned, the material was air-dried and ground into a fine powder. To create the hydrochar, we followed the established methodology of Li et al. [29] with minor modifications. Approximately 5 g of the powdered SB was combined with 100 mL of distilled water in a flask and placed in an autoclave for hydrothermal carbonization at 200 °C for 20 hours. The resulting slurry was then filtered and repeatedly rinsed with distilled water until the filtrate reached a neutral pH. The solid residue was oven-dried at 80 °C for 24 hours, after which it was ground into a fine powder using a Fritsch Pulverisette 16 cross-beater mill. The final

product was stored in an airtight container and labeled as raw sugarcane bagasse hydrochar (RSBH).

2.3 Activation of Sugarcane Bagasse Hydrochar

To enhance the material's porosity and surface area, two different activation treatments were applied to RSBH samples. For phosphoric acid activation, the RSBH powder was treated with phosphoric acid in a 2:1 weight ratio and left to activate for 15 hours at room temperature. Following activation, the mixture was filtered to remove any unreacted phosphoric acid and washed thoroughly with hot distilled water at 80 ℃ until the filtrate pH became neutral. After drying at 80 ℃ for 24 hours, this product was designated as phosphated sugarcane bagasse hydrochar (PSBH).

To improve hydrophilicity, a sulfonation treatment was performed on a separate batch of RSBH. The powder was refluxed with 120 mL of concentrated sulfuric acid at 150 ℃ for 6 hours to ensure thorough impregnation. Once the reaction was complete, the mixture was filtered to remove excess and unreacted sulfuric acid, followed by careful washing with hot distilled water at 80 ℃ until the filtrate pH reached neutral. The resulting solid was dried at 80 ℃ for 24 hours, producing the final sulfonated product, which was labeled as sulfonated sugarcane bagasse hydrochar (SSBH).

2.4 Characterization of hydrochars from sugarcane bagasse

2.4.1 Structural and morphological analyses

Comprehensive identification of functional groups was undertaken through Fourier-transform infrared (FTIR) spectroscopy (PerkinElmer, Wellesley, USA) spanning a wavenumber range of

4000-400 cm^{-1} [10]. The crystallinity was confirmed using X-ray diffraction analysis (Philips X'pert diffractometer) [30].

Morphological characterization of the hydrochar samples was conducted employing field emission scanning electron microscopy (FESEM; Nova Nanosem 230, Cranberry, PA, USA) integrated with energy-dispersive X-ray spectroscopy (EDX; Oxford Instruments, Max 20, Abingdon, UK) [31]. This coupled analytical approach enabled simultaneous correlation of observed morphological transformations with elemental composition, thereby furnishing direct evidence of carbon structure functionalization.

2.4.2 Thermal analysis

Thermal stability and compositional profiling of the hydrochars were evaluated through thermogravimetric analysis (TGA) using a Netzsch STA 449C instrument [30].

2.5 Application hydrochars as electrode modifier in microbial fuel cells (MFC)

2.5.1 Electrode preparation and modification

Nickel foam electrodes (2 × 3 cm^2) underwent purification through successive washing cycles with 3 M hydrochloric acid solution, followed by rinsing with ultrapure water (18.2 MΩ/cm resistivity). The electrodes were subsequently dried at 50 ℃ overnight in a desiccating oven prior to surface modification. Both anode and cathode electrodes were fabricated using the doctor blade coating technique, a well-established methodology in electrode preparation [32, 33]. The electrode surfaces received a composite coating consisting of 20 mg of active material (RSBH, PSBH, and SSBH) combined with 100 µL of polytetrafluoroethylene (PTFE) binder. These preparations were

designated Ni-RSBH, Ni-PSBH, and Ni-SSBH, respectively. Multiwalled carbon nanotube (CNT) was coated on nickel foam following the earlier mentioned procedures to serve as control electrode (Ni-CNT). All coated electrodes underwent a secondary drying step at 50 ℃ for 4 hours and were subsequently stored in airtight containers until experimental use.

2.5.2 MFC assembly and operation

MFC apparatus consisted of two 700 mL polyvinyl chloride containers configured in an H-shaped dual-chamber design through connection using a 5 cm-diameter PVC union connector containing a Nafion 117 ion-exchange membrane [5]. The anode chamber was populated with laboratory-synthesized anolyte [8], while the cathode chamber contained 600 mL of 0.05 M potassium ferricyanide in 0.1 M phosphate buffer solution. The total anolyte volume comprised 600 mL supplemented with 10 % (*v/v*) bacterial inoculum (*Bacillus albus* TAJ01) as the biocatalyst [34]. The anode compartment was initially sparged with purified nitrogen gas to maintain anaerobic conditions, whereas the cathode compartment received purified oxygen to establish oxygen-saturated conditions. The anode and cathode electrodes were the hydrochar-coated electrodes (Ni-RSBH, Ni-PSBH, and Ni-SSBH), while Ni-CNT served as the control electrode.

Voltage monitoring was conducted at 30-minute intervals over a 55-day operational period at 30 ℃ ± 2 ℃ using an automated data acquisition system (Keysight DAQ970A). Following attainment of stable voltage output, power and current densities were calculated normalized to the anode surface area while systematically varying the external resistance between 55 Ω and 10,000 Ω [35].

2.5.3 Electrochemical analyses

Prior to MFC operation, the modified electrodes underwent electrical conductivity assessment using electrochemical impedance spectroscopy (EIS) conducted with a precision impedance analyzer (HIOKI 3532-50 LCR HiTESTER, Japan). The electrodes were positioned between metal plates (3.142 cm^2 contact area) for measurement. Cole-Cole plots were generated for each electrode through EIS measurements conducted at frequencies ranging from 100 Hz to 1 MHz with a 10 mV alternating current amplitude [36, 37].

Cyclic voltammetry (CV) measurements were performed on anode electrodes (prior to biofilm development) in the laboratory-synthesized anolyte containing biocatalyst, while cathode electrode characterization was conducted in three distinct electrolytic media: potassium ferricyanide solution, 0.5 M potassium hydroxide, and oxygen-saturated deionized water. Both CV and EIS (Nyquist plot) measurements were recorded when the MFC system reached a stable state conditions and upon experiment termination using a potentiostat (Autolab PGSTAT 204, B.V., Netherlands). Cyclic voltammograms were acquired at a scan rate of 10 mV/s across a potential window of -1 V to +1 V, employing Ag/AgCl and platinum wire as reference and counter electrodes, respectively, with the hydrochar-coated electrodes serving as working electrodes. Electrode capacitance values were calculated from the CV curves using established computational protocols [38, 39]. Electrochemical impedance spectra were acquired in open-circuit mode across frequencies spanning 0.05 Hz to 100 kHz. For anode electrode characterization, the cathode electrode functioned simultaneously as both reference and counter electrode, and *vice versa* for cathode electrode analysis.

3. Results and Discussion

3.1 Structural and morphological analyses

The FTIR spectra of RSBH, PSBH, and SSBH preparations as shown in Fig. 1 provide clear evidence of structural modifications following acid functionalization. All three hydrochar samples exhibit a broad absorption band in the region of 3200-3600 cm^{-1}, which corresponds to O-H stretching vibrations of hydroxyl group. While this band is present in the RSBH spectrum, both PSBH and especially SSBH show significantly enhanced intensity in this region, reflecting increased surface hydrophilicity from the introduction of phosphate and sulfonic acid groups, which promote hydrogen bonding and water retention [40]. Weak absorptions in the 2900-2850 cm^{-1} region associated with aliphatic C-H stretching become slightly diminished after chemical treatment, indicating partial degradation or oxidation of residual aliphatic moieties during acid-mediated functionalization [41]. In the carbonyl region (1750-1650 cm^{-1}), RSBH shows a small shoulder attributed to C=O stretching in carboxylic and conjugated carbonyl species. This feature becomes more distinct in PSBH and SSBH, suggesting that acid treatment promotes oxidation and generates additional carbonyl or carboxyl functionalities on the hydrochar surface. Characteristic aromatic C=C stretching near 1600 cm^{-1} is present in all samples, corroborating the retention of the aromatic carbon framework typical of hydrochar structures [42]. However, the most significant changes occur in the 1300–900 cm^{-1} region. In PSBH, intensified peaks near 1180-1000 cm^{-1} correspond to P=O and P-O-C stretching vibrations, authenticating successful phosphorylation of the hydrochar materials. These bands are absent or weak in RSBH but become prominent following phosphoric acid treatment, indicating the formation of phosphate esters or surface-bound phosphate groups.

SSBH displays the most dramatic spectral transformation, with very strong absorptions between 1220 and 1030 cm^{-1} assigned to S=O asymmetric and symmetric stretching of $-SO_3H$ groups. The large increase in absorbance across this region, along with a more intense O-H band, substantiates

extensive sulfonation and the introduction of strongly acidic sulfonic species. Overall, the spectra of PSBH and SSBH preparations clearly demonstrate that both phosphoric and sulfuric acid treatments successfully functionalize the RSBH, but the extent and nature of chemical modifications differ substantially. PSBH material shows moderate incorporation of phosphate groups, while SSBH material exhibits extensive sulfonic group formation, abundant oxidation, and superior surface polarity. These chemical transformations are expected to significantly influence the properties and functions of the hydrochars in MFC.

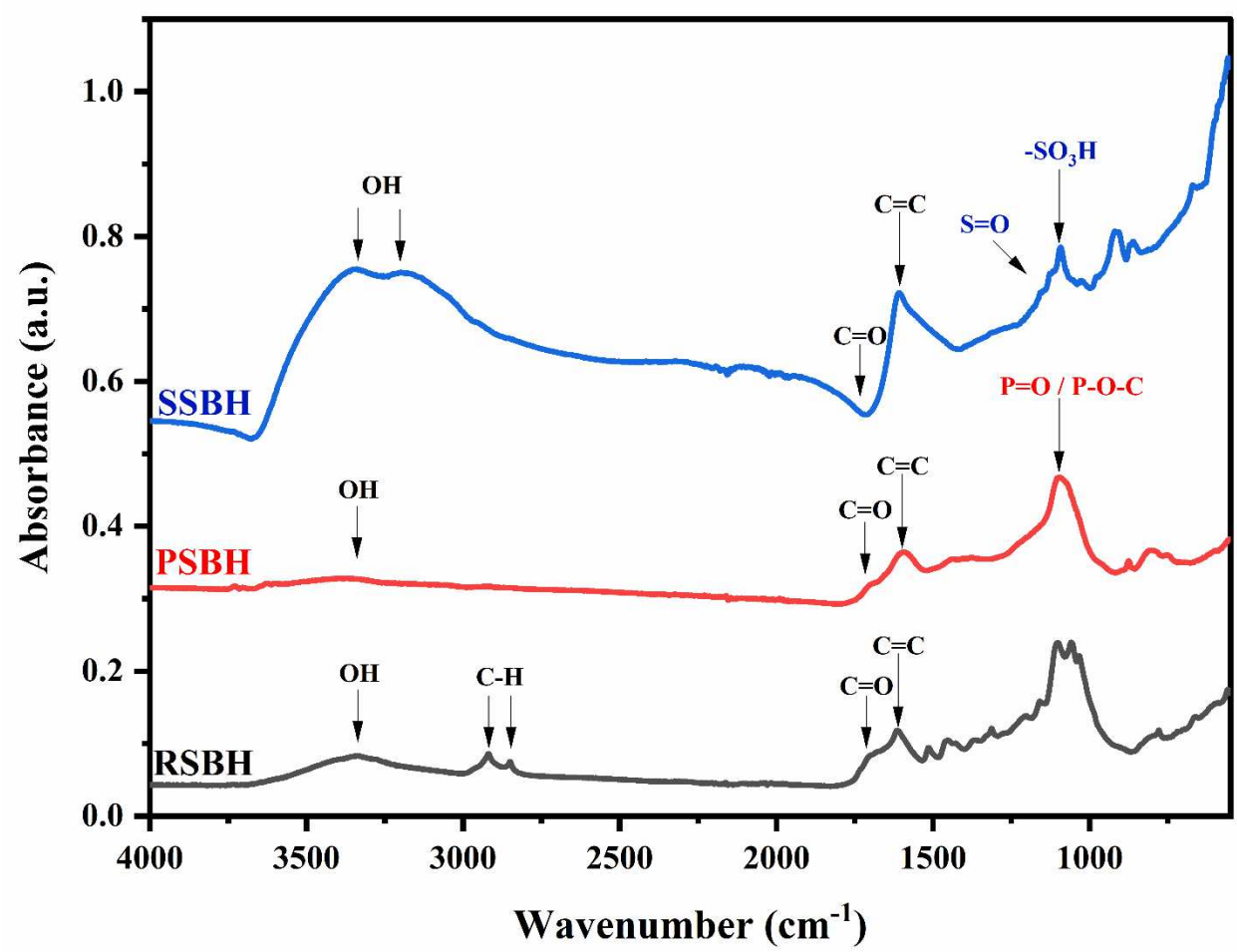

Fig. 1 FTIR spectra of RSBH, PSBH and SSBH preparations

The XRD analysis shows that the different hydrochar preparations are predominantly amorphous carbonaceous materials, as evidenced by their broad diffraction features and diffused background, upon which minor crystalline domains are superimposed (Fig. 2). Specifically, the RSBH material exhibits a diffraction pattern with low-intensity, broad peak centered around $2\theta = 22°$, a position corresponding to the (003) reflection of microcrystalline graphite [43]. This indicates the presence of some graphitized regions, yet the overall structure points to poor crystallinity, where the pronounced breadth and weak intensity of the peak are direct consequences of a highly disordered carbon structure, a hallmark of chars produced *via* low-temperature hydrothermal carbonization [44]. Following acid functionalization, both PSBH and SSBH materials retain this fundamental amorphous character, but their diffraction profiles show distinct, minor modifications. PSBH demonstrates a slight increase in peak intensity, with the peak shifting to approximately $2\theta = 24°$, a change that could point to a marginal enhancement in local graphitic ordering or potentially to the presence of residual crystalline phosphate phases [45]. In contrast, SSBH exhibits the broadest and significantly repressed diffraction peaks of the investigated set, signaling a further destruction of short-range order and a heightened state of amorphization resulting from the aggressive sulfonation process [46]. Ultimately, the persistent peak broadening and the consistent absence of sharp crystalline reflections across all three samples confirmed the dominance of structural disorder and infer that the development of extensive crystalline domains is severely curtailed, with the minor crystalline signals likely originating from small graphitic clusters or inorganic residues such as phosphate in PSBH or sulfate in SSBH materials [44].

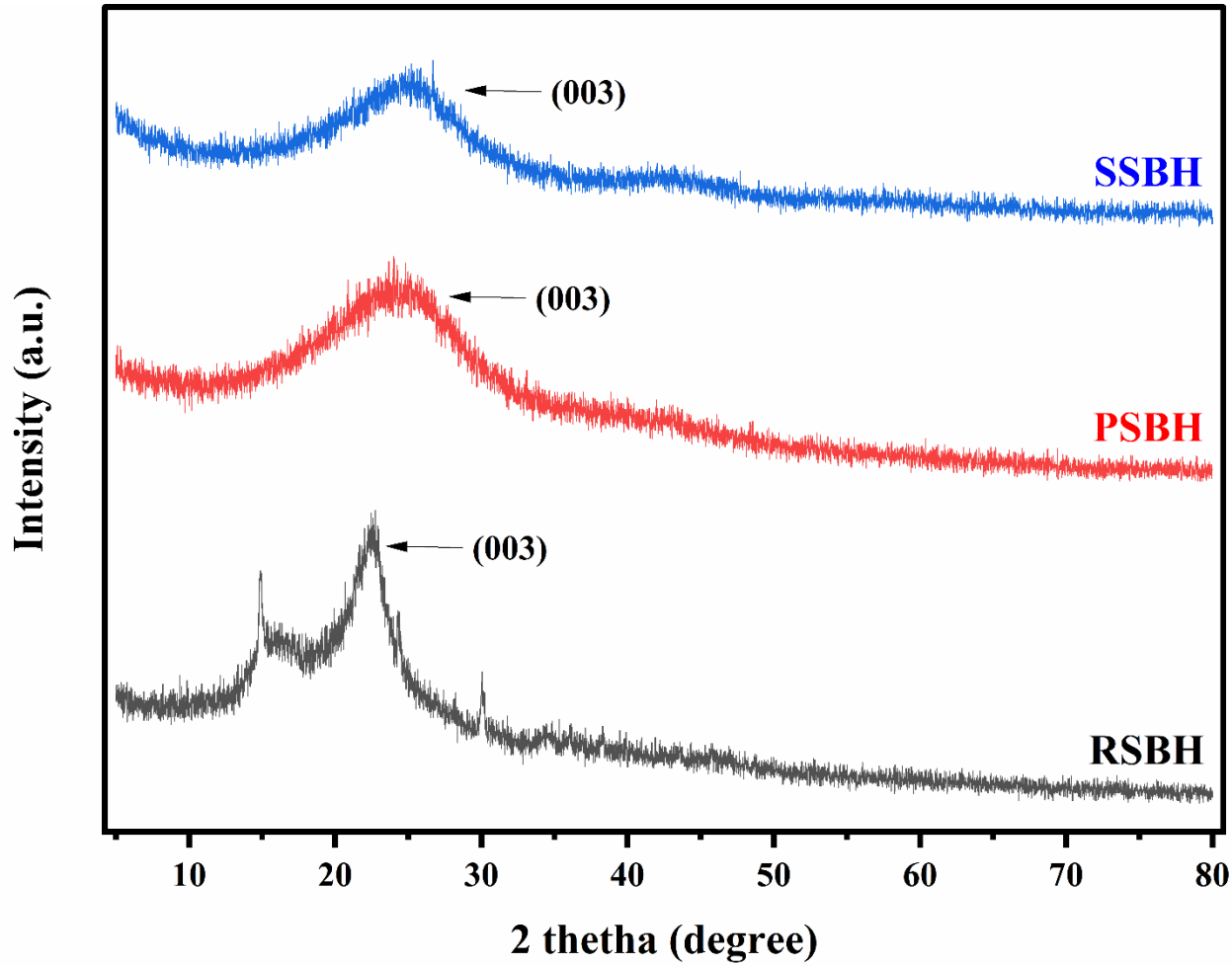

Fig. 2 X-ray diffraction patterns of RSBH, PSBH and SSBH preparations

The morphological changes in the raw hydrochar samples resulting from chemical modifications is presented in Fig. 3 at 1 µm magnification (FESEM). The RSBH preparation exhibits a disordered, highly porous carbon matrix composed of aggregated, submicron spheroidal particles, forming an open, three-dimensional network with abundant interparticle voids, which is typical for materials produced from untreated biomass (Fig. 3(a)) [47, 48]. In contrast, Fig. 3(b) displays PSBH surface with a more compact, plate-like morphology, with stacked lamellar domains and partially fused particles that create interconnected ridges and terraces, indicating phosphate-induced restructuring and densification of the hydrochar framework. Sulfonated hydrochar (SSBH,

Fig. 3(c)) morphology retains a granular appearance but with more fused and coalesced particles, yielding a rough, nodular surface texture characterized by irregular clusters and narrowed pore throats, consistent with extensive sulfonation and surface cross-linking [49, 50].

Complementing the morphological observations, the EDX spectra authenticate the incorporation of new functional elements following chemical treatments (Fig. 3(d-f)). The RSBH preparation presents significant carbon and oxygen peaks, consistent with its organic composition, and a minor silicon signal from residual biomass ash (Fig. 3(d)). The phosphated hydrochar, PSBH distinctly features a phosphorus peak alongside C, O, and Si, validating the presence of phosphate groups (Fig. 3(e)). Sulfonated hydrochar, SSBH shows a clear sulfur peak in addition to C, O, and Si, validating successful sulfonation (Fig. 3(f)). These compositional modifications, evident from both FESEM and EDX analyses, demonstrated that phosphate and sulfonic group treatments modified the hydrochar's structure and elemental makeup for specific potential applications.

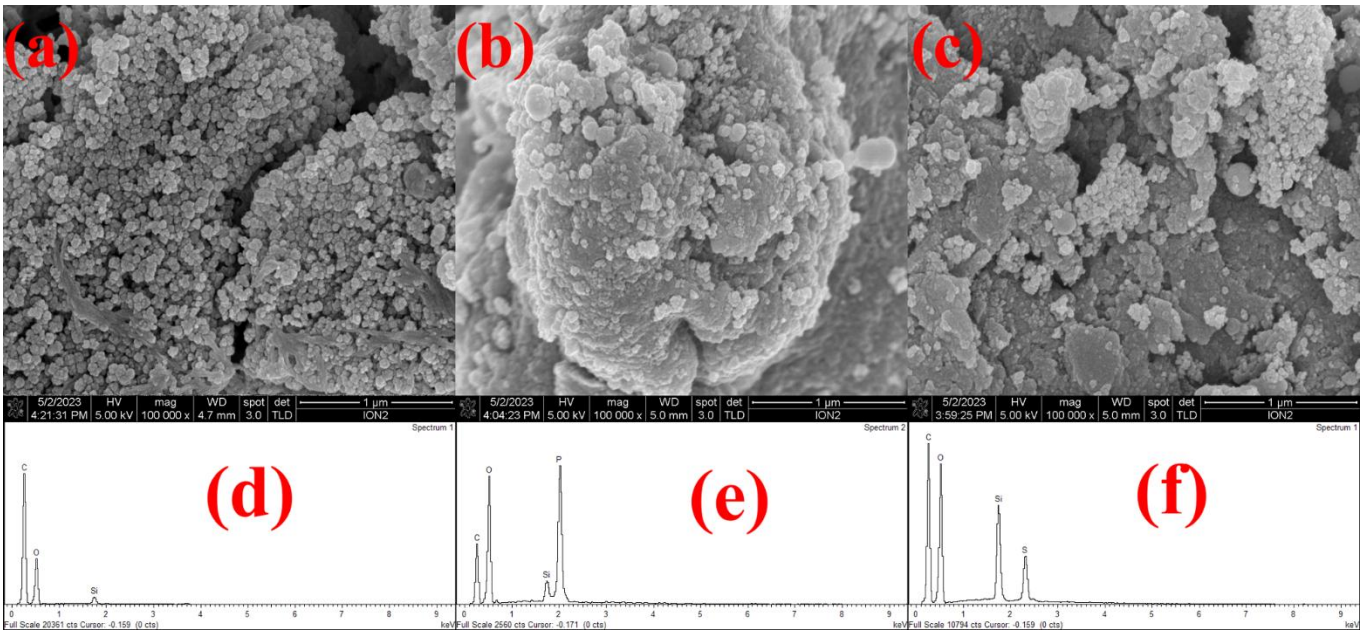

Fig. 3 FESEM images of (a) RSBH, (b) PSBH (c) SSBH at 1 μm, and EDX spectra of (d) RSBH, (e) PSBH (f) SSBH

3.2 Thermal analysis

The thermal properties of RSBH, PSBH, and SSBH were investigated using TGA analysis (Fig. 4). Collectively, the thermograms show phosphation and sulfonation significantly restructure the raw hydrochar material, redistributing mass loss among dehydration and devolatilization stages while enhancing final char yield and apparent thermal stability. RSBH material exhibits modest moisture loss of about 4.9 wt% between 25 and 150 ℃, and a much larger mass loss of roughly 40.6 wt% in the 300 – 500 ℃ range, with a dominant derivative thermogravimetry (DTG) peak at around 368 ℃, which is typical of bulk decomposition of residual cellulose, hemicellulose, and less-condensed lignin domains imparting some degree of thermolability in the raw hydrochar [51]. In contrast, PSBH and SSBH materials display considerable low-temperature losses (16.9 and 14.3 wt% at 25 – 150 ℃, respectively) and substantial additional losses in 150 – 300 ℃ (12.9 and 9.6 wt%), accompanied by strong DTG peaks at only around 70 – 80 ℃, indicating intense acid-catalyzed dehydration and removal of absorbed water and labile oxygenated groups formed during acid treatment [52, 53]. This early devolatilization, together with the strongly reduced 300 – 500 ℃ mass loss in PSBH (9.9 wt%) and SSBH (14.5 wt%) materials, supports that phosphoric and sulfuric acids promote extensive condensation and cross-linking of carbohydrate fragments into abundant aromatic, thermally robust networks before high-temperature decomposition occurs [54]. The main decomposition window for the treated char samples still initiates around 200 ℃, but main event for PSBH material ended earlier (436 ℃) than RSBH and SSBH (both near 500 ℃), consistent with the formation of phosphate-stabilized char structures that devolatilize over a

narrower temperature range [53, 54]. The apparently higher final residues of PSBH (46.5 wt%) and SSBH (46.3 wt%) compared with RSBH (38.9 wt%) suggests that both phosphation and sulfonation act as char-promoting treatments. Phosphates are classically associated with flame retardancy and enhanced char yield, while sulfonic functionalities encourage dehydration and aromatic ring formation but also introduce sulfur-containing moieties that decompose over a broader 300–700 ℃ window, giving SSBH material a somewhat more complex, multi-step DTG pattern than PSBH [51, 55]. Overall, the combined shifts in moisture loss, DTG peak positions, decomposition ranges, and residue percentages justify the conclusion that acid modification converts a largely polysaccharide-dominated RSBH into phosphorus- or sulfur-stabilized hydrochars with higher fixed-carbon content, stronger cross-linking, and improved resistance to high-temperature mass loss, which is advantageous for applications requiring thermally stable, carbon-rich electrode materials.

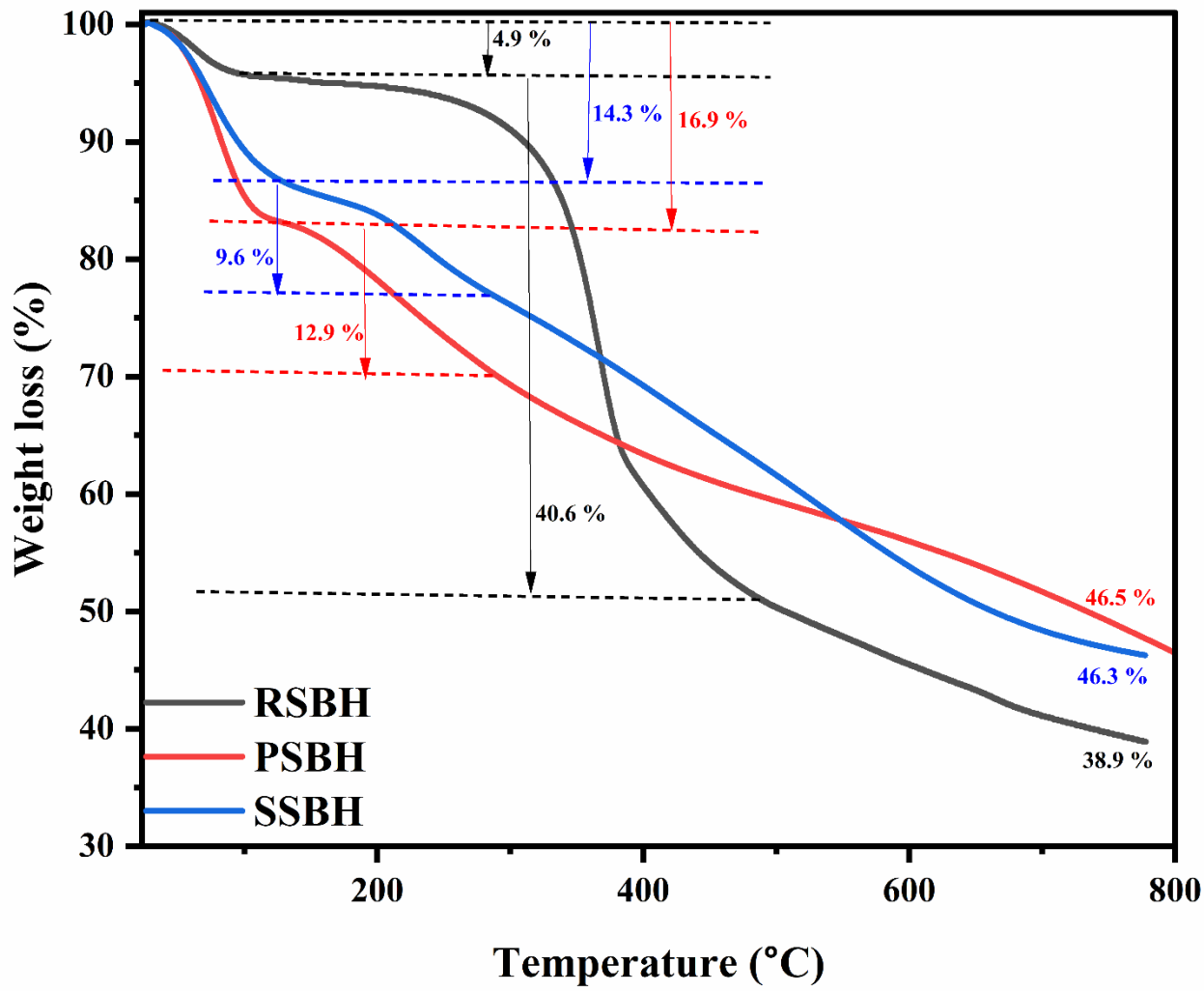

Fig. 4 Thermograms of RSBH, PSBH and SSBH preparations

3.3 Hydrochars application in microbial fuel cell

3.3.1 Power output

Over 56 days of operation, all four MFC setups produced stable voltages, but with a performance order of Ni-PSBH > Ni-CNT > Ni-RSBH > Ni-SSBH (Fig. 5). At start-up (day 1), Ni-RSBH showed the highest initial voltage (0.77 ± 0.25 V), slightly above Ni-PSBH (0.69 ± 0.31 V), while Ni-SSBH and Ni-CNT were lower at 0.63 ± 0.13 V and 0.62 ± 0.26 V, indicating faster but less uniform initial activation of the RSBH on nickel foam surface compared with the acid-treated

electrodes. By day 2, Ni-PSBH sharply overtook the others, rising to 0.92 ± 0.01 V compared to 0.87 ± 0.07 V (Ni-RSBH), 0.82 ± 0.02 V (Ni-CNT), and 0.54 ± 0.02 V (Ni-SSBH), and then maintained the highest and most stable voltage (typically 0.68–0.71 V with very low standard deviations on the order of 0.001 – 0.006 V) throughout the middle of the run, attributed to the well-established biofilm colonization of the electrode surface (Fig. 6). Ni-CNT consistently delivered intermediate but robust voltages (between 0.60 – 0.77 V), surpassing Ni-RSBH (0.49 – 0.69 V) and Ni-SSBH (0.49 – 0.59 V). The relatively poor and more fluctuating voltages of Ni-SSBH, particularly at early and late stages where it often remained below 0.55 V and declined toward 0.43 – 0.45 V, suggest that sulfonation introduces strongly acidic groups that are less compatible with neutral-pH MFC operation, destabilizing the anodic biofilm and increasing cathodic overpotentials (Fig. 6c and 6d) [56, 57]. In contrast, phosphation in Ni-PSBH appears to yield higher absolute voltages, indicative of a more homogeneous and electrochemically stable electrode surface than in Ni-RSBH and Ni-SSBH, while CNT reinforcement in Ni-CNT provides superior electronic pathways but fewer chemically tailored sites, leading to performance slightly below Ni-PSBH yet clearly above Ni-RSBH and Ni-SSBH over the entire 56-day operation.

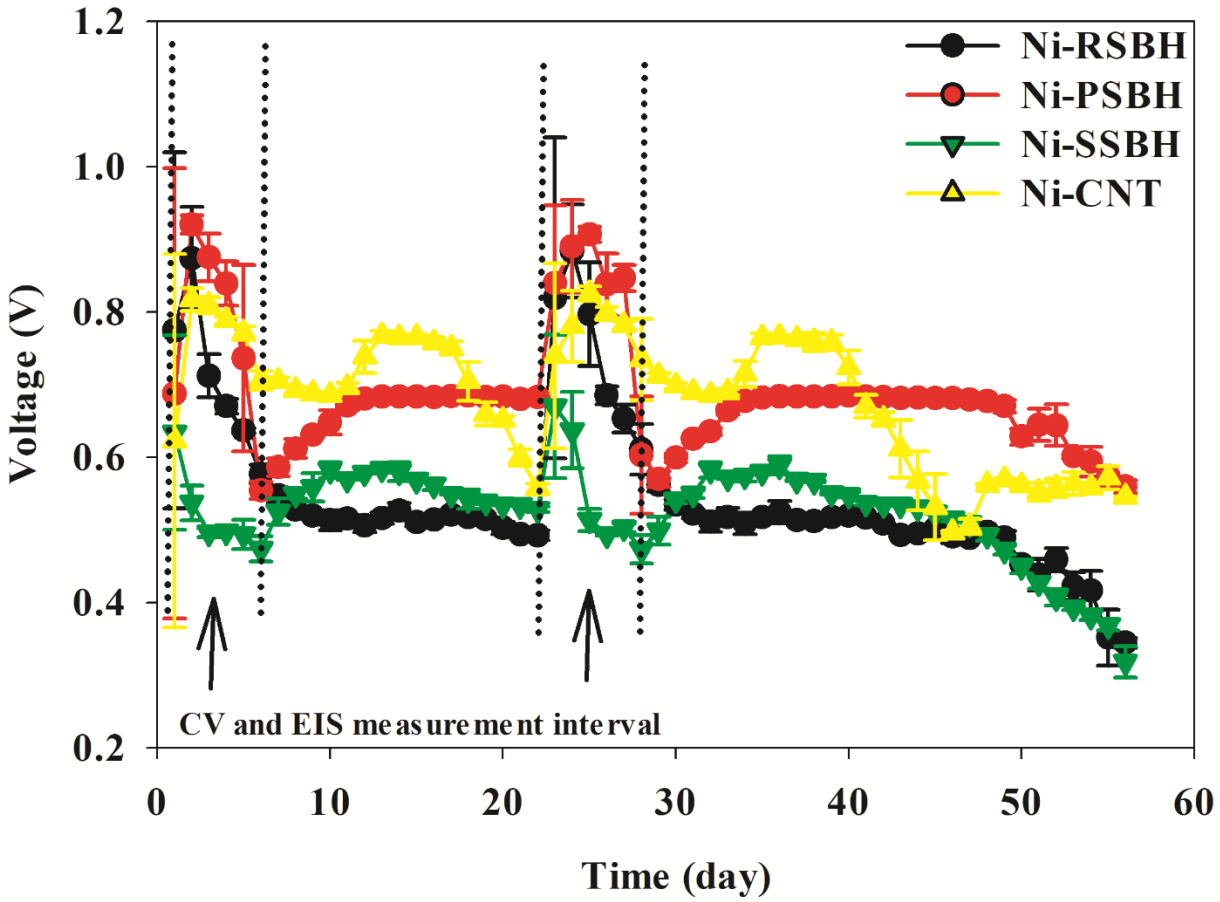

Fig. 5 Voltage measurement across 56 days of MFC operation applying Ni-RSBH, Ni-PSBH, Ni-SSBH and Ni-CNT electrodes

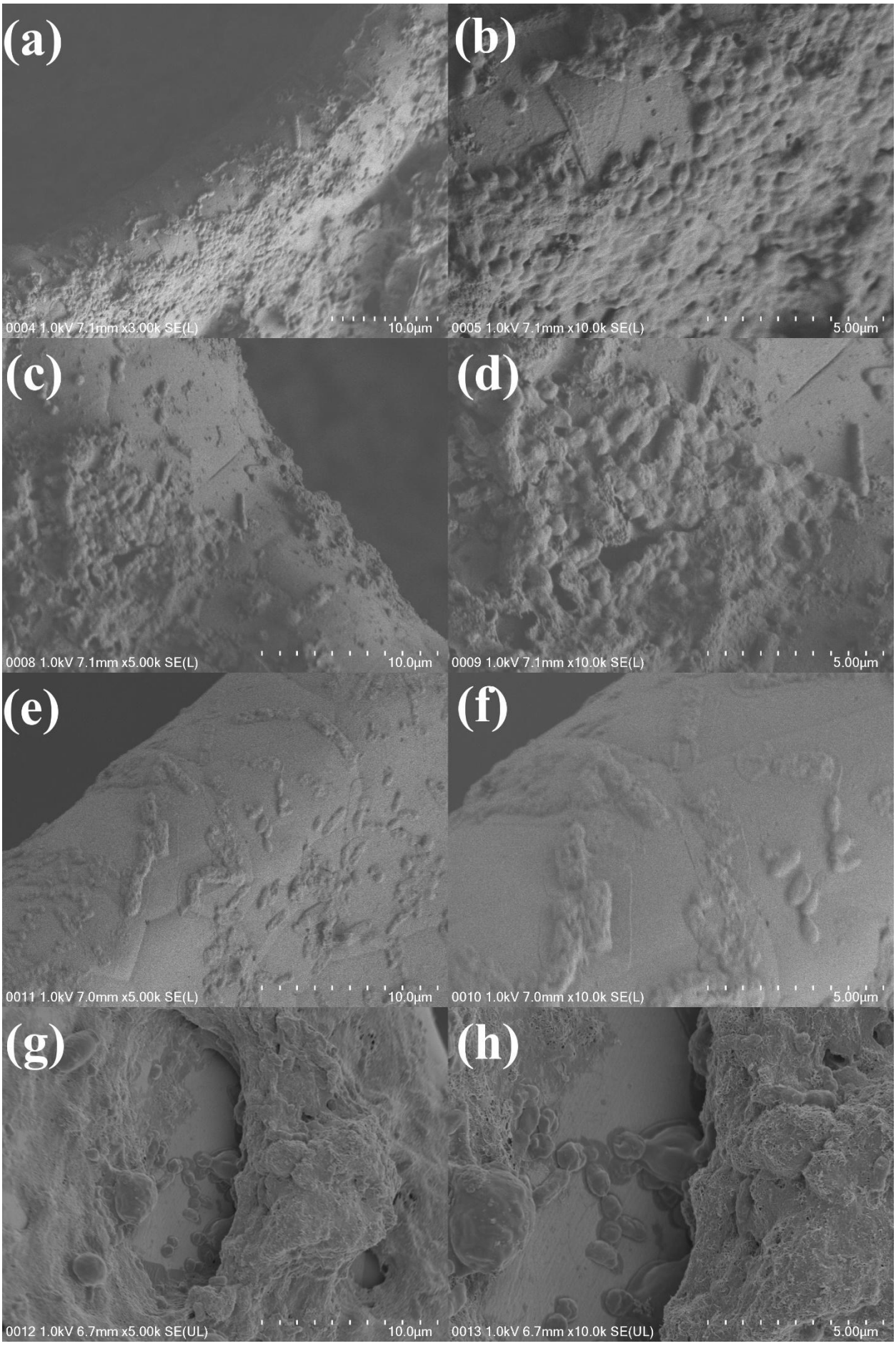
(a)
0004 1.0kV 7.1mm x3.00k SE(L)
10.0µm
(b)
0005 1.0kV 7.1mm x10.0k SE(L)
5.00µm
(c)
0008 1.0kV 7.1mm x5.00k SE(L)
10.0µm
(d)
0009 1.0kV 7.1mm x10.0k SE(L)
5.00µm
(e)
0011 1.0kV 7.0mm x5.00k SE(L)
10.0µm
(f)
0010 1.0kV 7.0mm x10.0k SE(L)
5.00µm
(g)
0012 1.0kV 6.7mm x5.00k SE(UL)
10.0µm
(h)
0013 1.0kV 6.7mm x10.0k SE(UL)
5.00µm

Fig. 6 FESEM images showing bacterial biofilm formation for (a) Ni-RSBH at 10 µm, (b) Ni-RSBH at 5 µm, (c) Ni-PSBH at 10 µm, (d) Ni-PSBH at 5 µm, (e) Ni-SSBH at 10 µm, (f) Ni-SSBH at 5 µm, (g) Ni-CNT at 10 µm, (h) Ni-CNT at 5 µm

Across the polarization curves of the four MFCs, Ni-RSBH delivered the highest maximum power density (PD), followed by Ni-PSBH, Ni-CNT and finally Ni-SSBH (Fig. 7). For Ni-RSBH, power density increased from 200 mW/m^2 at 1602.6 mA/m^2 current density (CD), to a maximum of 1008 mW/m^2 at 2328 mA/m^2 before declining at higher current densities, indicating that Ni-RSBH electrodes supports relatively high reaction rates but experiences growing ohmic and diffusion limitations beyond this optimum [58, 59]. Ni-PSBH showed a lower maximum PD of 347 mW/m^2 at 1366 mA/m^2 compared to Ni-RSBH, yet with the absence of drastic current reversal, suggesting that phosphation moderates current output but improves the uniformity of active sites and limits excessive polarization at higher loads [60]. The CNT-based electrodes (Ni-CNT) reached a maximum power density of 235 mW/m^2 at 1400 mA/m^2, reflecting the benefit of CNT in enhancing electronic conductivity and efficient charge transport, although its PD and CD remained below Ni-RSBH. In contrast, Ni-SSBH produced the lowest maximum PD, only about 94 mW/m^2 at 465 mA/m^2, which could be attributed to the strongly acidic sulfonated material that hinders both electron transfer and effective bioelectrocatalytic activities. While surface functionalization can stabilize performance and improve conductivity, excessive sulfonation could be detrimental to the anode, and the Ni-RSBH setup still provides the most efficient combination of accessible active sites and mass transport under the studied conditions.

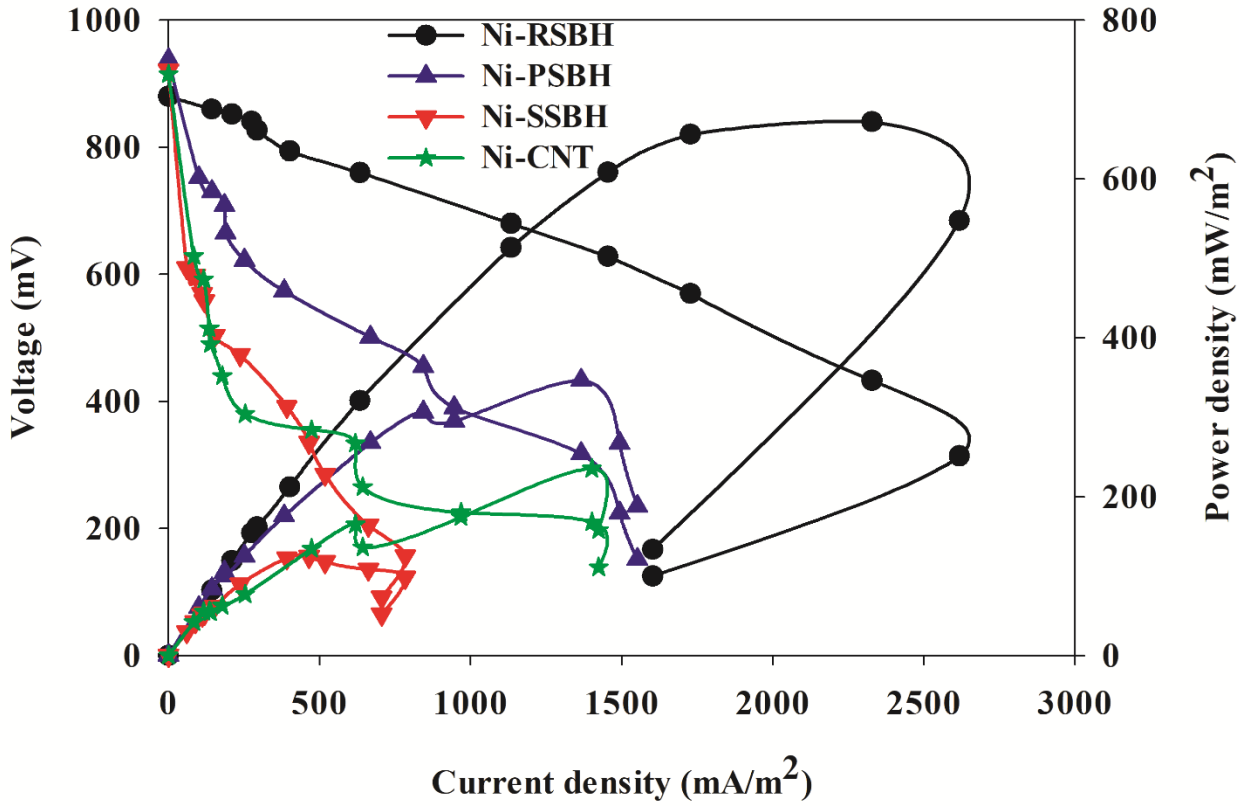

Fig. 7 Power and current densities recorded by MFC setup with Ni-RSBH, Ni-PSBH, Ni-SSBH and Ni-CNT electrodes

3.3.2 Cyclic voltammetry (CV) measurement for anode electrodes

Prior to the start of MFC operation, the electrodes were subjected to CV to investigate the electrodes' pre-colonization electrochemical behaviors in the presence of *B. albus* TAJ01 suspension as biocatalyst (Fig. 8). Ni-RSBH (Fig. 8(a)) and Ni-PSBH (Fig. 8(b)) exhibit relatively low currents in the 10^{-5} A range across the scanned potential window, with nearly linear increases in current as potential becomes more positive, indicating predominantly electric double-layer charging with limited biocompatibility to the biocatalyst. The slightly higher currents of Ni-RSBH compared with Ni-PSBH at the same potentials suggest that the RSBH material offers more

accessible conductive pathways or higher electroactive area to the bacterial culture, whereas phosphate functionalization in PSBH moderates the response by partially reorganizing the active sites, producing a more controlled but less intense pseudocapacitive behavior [61]. In contrast, Ni-SSBH (Fig. 8(c)) and Ni-CNT (Fig. 8(d)) display much larger absolute currents with Ni-SSBH reaches about -1.3×10^{-3} A in the negative potential region and transitions to positive currents on the order of 10^{-4} – 10^{-3} A, typical redox for sulfur-related surface processes [62], while Ni-CNT shows the highest positive currents, rising from around 7.5×10^{-4} A to above 2.0×10^{-3} A due to the high initial biocompatibility of CNT with the biocatalyst [63]. Although, Ni-CNT and Ni-SSBH are intrinsically more electroactive prior to biofilm colonization of the electrode, however, Ni-RSBH and especially Ni-PSBH behave more like stable pseudocapacitive electrodes, which consequently favor sustained, biofilm-mediated current generation in MFCs by providing a less aggressive but electrochemically supportive interface.

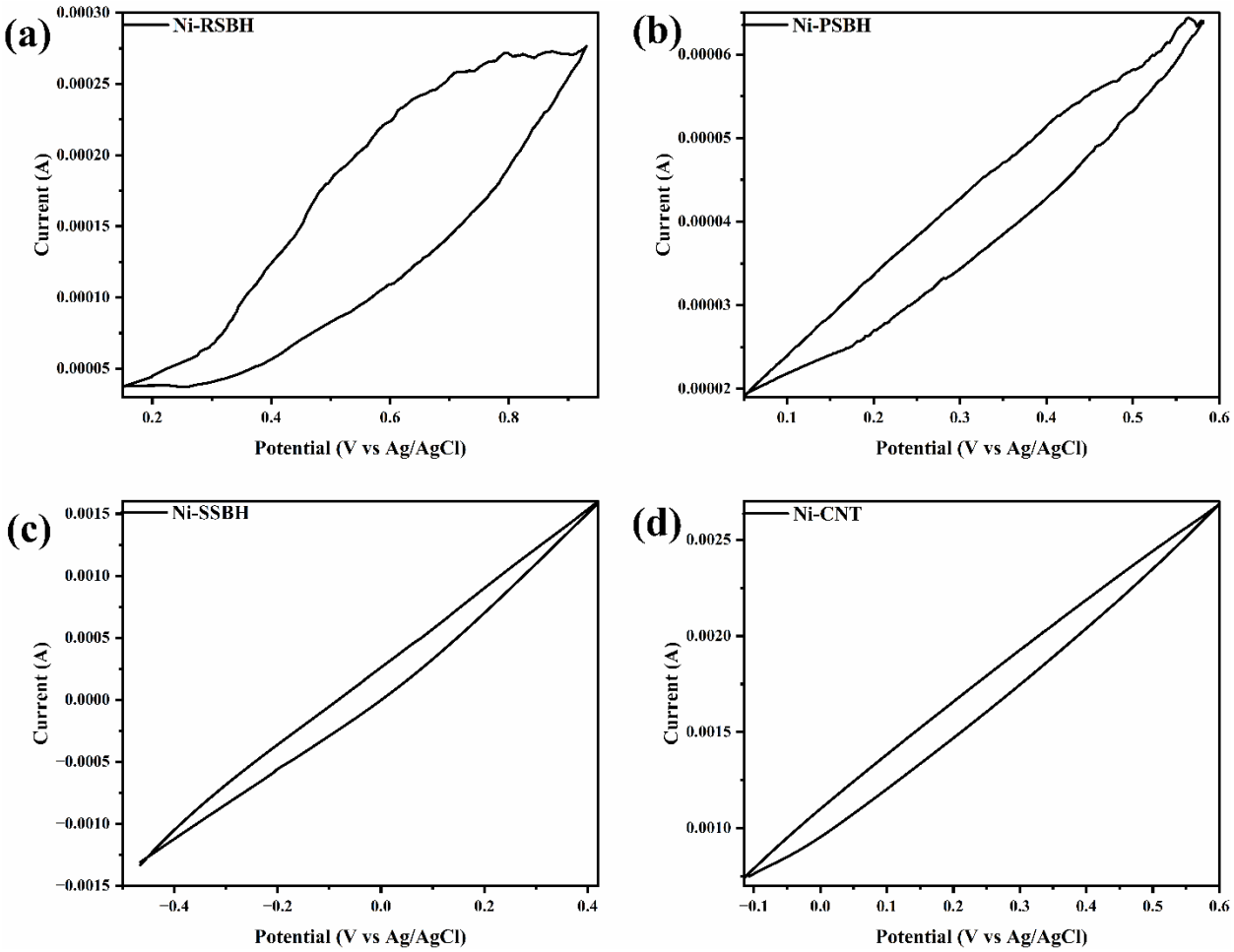

Fig. 8 CV curves of (a) Ni-RSBH, (b) Ni-PSBH, (c) Ni-SSBH and (d) Ni-CNT anode electrodes in lab-prepared anolyte with *B. albus* TAJ01 as biocatalyst prior to MFC application

After extended MFC operation and biofilm formation, the electrodes were once again subjected to CV analysis (Fig. 9). A clear confirmation and enhancement of the trends anticipated from their pre-MFC behavior, showing how initial electrochemical properties translate into mature bioelectrode performance. Ni-RSBH in Fig. 9(a) shows a substantial increase in current from the pre-colonization 10^{-5} A level into the 10^{-2} A range, indicating that RSBH material provides a highly supportive scaffold for dense bacterial attachment (Fig. 6(b)) and efficient extracellular electron transfer once the biofilm is fully established, despite its initially modest capacitive response. Ni-

PSBH in Fig. 9(b), which previously displayed slightly lower currents than Ni-RSBH due to phosphate-induced moderation of active sites, now develops a well-defined, faradaic envelope with currents growing from around 1.5×10^{-3} A to about 5×10^{-3} A across the same potential window, reflecting a synergistic interaction between the stabilized, phosphate-functionalized surface and the mature biofilm (Fig. 6(d)) that enhances pseudocapacitive storage and redox-mediated electron shuttling at the cell–electrode interface [61]. In contrast, Ni-SSBH, although intrinsically electroactive before colonization, shows moderate biotic currents (-1.4×10^{-3} to 3.3×10^{-3} A, Fig. 9(c)), implying that the strongly acidic sulfonic groups and associated sulfur redox processes are less favorable for stable, thick biofilm formation as indicated by the scarce biofilm colonization in Fig. 6(f)), arguably from local pH disturbances and less biocompatible surface chemistry that curtail microbially driven redox turnover. Ni-CNT, which initially exhibited the highest currents due to the highly conductive CNT backbone now displays a more moderated but still significant biotic response (currents rising from about -1.1×10^{-3} to 2.0×10^{-3} A, Fig. 9(d)), suggesting that while CNTs promote early-stage bacterial adhesion and rapid electron transport, the long-term biofilm architecture and metabolic activities distribute more evenly across Ni-RSBH and Ni-PSBH materials which better accommodates dense, metabolically active biofilm (Fig. 6).

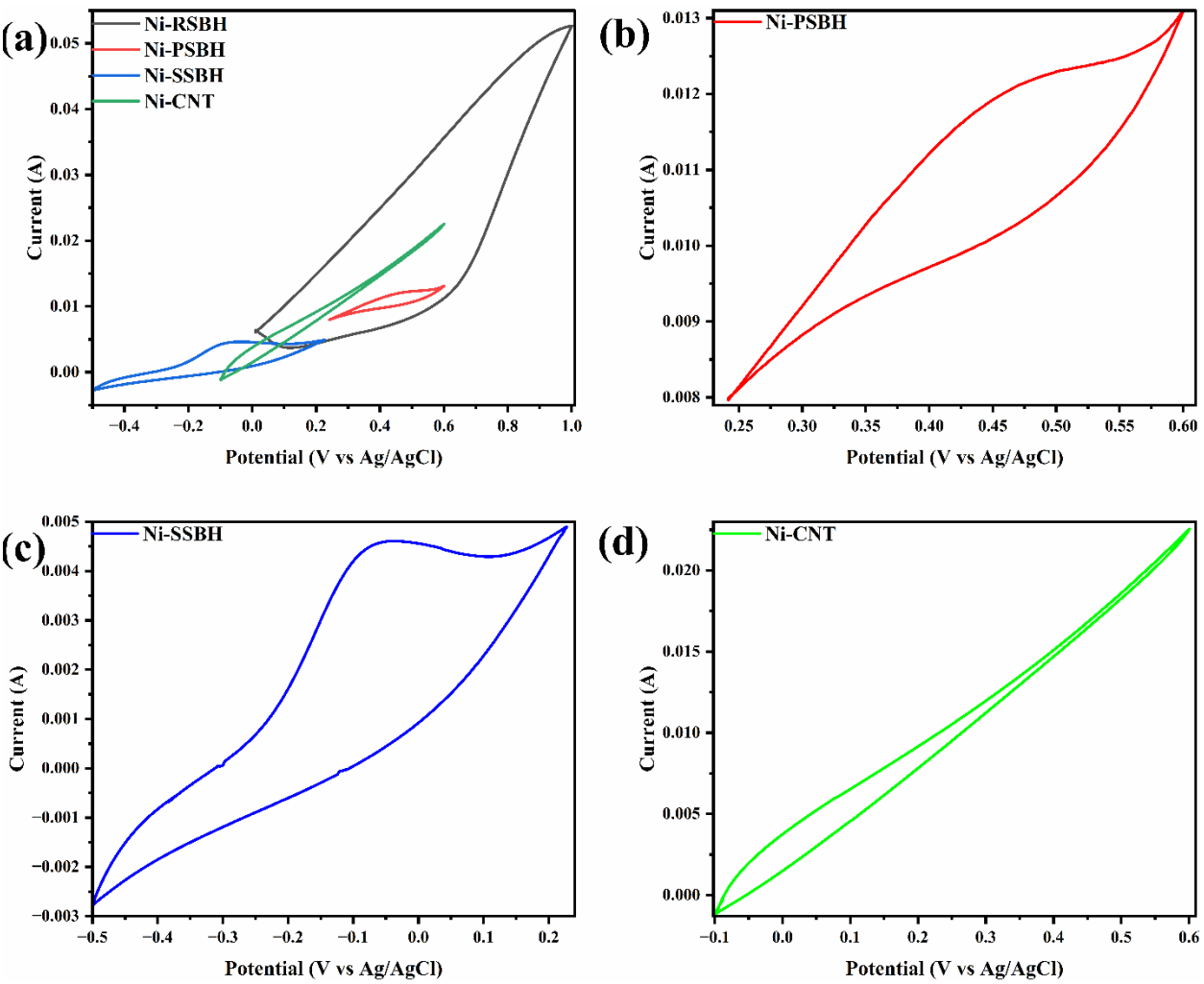

Fig. 9 CV curves of (a) Ni-RSBH, (b) Ni-PSBH, (c) Ni-SSBH and (d) Ni-CNT anode electrodes in lab-prepared anolyte with *Bacillus albus* TAJ01 as biocatalyst during MFC operation (after biofilm colonization of the electrodes)

To assess the sustainability, reusability, and electrochemical stability of the anode electrodes, cyclic voltammetry (CV) was performed after 56 days of MFC operation (Fig. 10). Ni-RSBH displays quasi-rectangular, pseudocapacitive loops with the highest currents ranging from 0.005 to 0.05 A across 0–1 V, confirming that the RSBH and biofilm–electrode interface remains electrochemically stable and reusable even after nearly two months of use (Fig. 10(a)). Ni-PSBH

demonstrates stable and reproducible behavior, with currents steadily rising from 0.008 to 0.013 A over 0.25–0.60 V and absence of distortion in the CV profile, indicating that phosphate functionalization effectively stabilizes active sites and biofilm attachment (Fig. 6), resulting in superior long-term durability (Fig. 10(b)). Conversely, Ni-SSBH shows the lowest current range between -0.0028 and 0.0048 A over -0.5 to 0.2 V, reflecting greater performance degradation and less consistent faradaic responses, consistent with its more aggressive initial redox activity and weaker long-term biofilm–electrode interaction (Fig. 10(c)). Although Ni-CNT exhibits improved performance compared to its initial and during-MFC operation states i.e., currents between -0.020 and 0.025 A over -0.1 to 0.6 V (Fig. 10(d)), it still falls significantly short of Ni-RSBH, highlighting the superior performance of the raw hydrochar relative to industrial-grade, highly purified CNT.

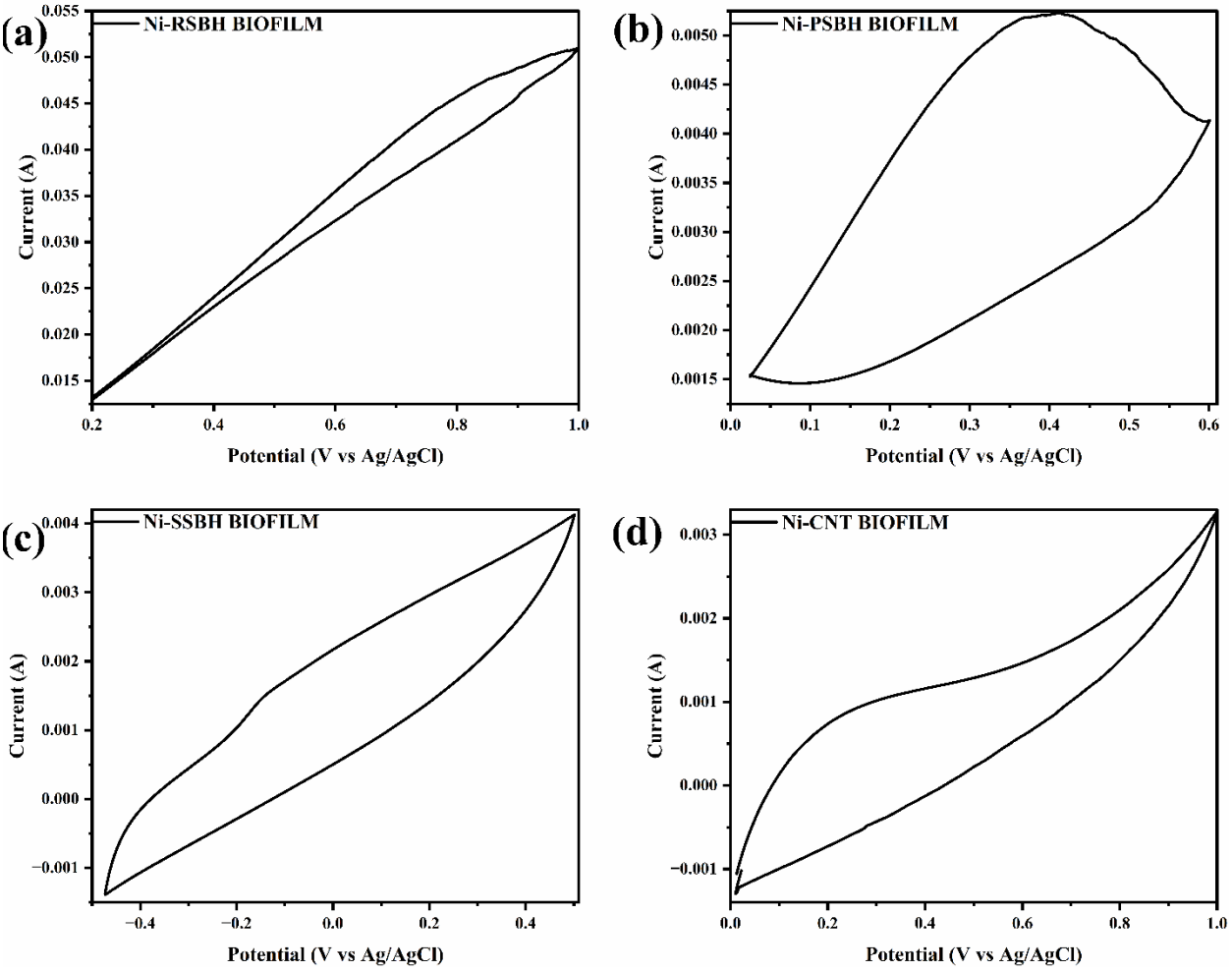

Fig. 10 CV curves of (a) Ni-RSBH, Ni-PSBH, Ni-SSBH and Ni-CNT anode electrodes in lab-prepared anolyte with *Bacillus albus* TAJ01 as biocatalyst post MFC operation, while (b), (c) and (d) represent the enhanced curves of Ni-PSBH, Ni-SSBH and Ni-CNT respectively

Table 1 shows the electrical conductivities of the anode electrodes and the specific capacitances recorded before-, during- and after MFC operation. Despite similar conductivities, the four anodes showed very different capacitance evolution that mirrors their CV behavior and biofilm interactions. Ni-RSBH transforms from a low pre-MFC capacitance (0.49 F/g) to very high values during (8.39 F/g) and especially after MFC operation (51.03 F/g), consistent with its initially mild, capacitive CV evolving into large biofilm-driven pseudocapacitive envelopes and excellent

charge-storage sustainability. Ni-PSBH, although highly stable in CV, exhibits a very low pre-MFC capacitance (0.05 F/g) and only moderate values during- (6.11 F/g) and post-MFC (3.54 F/g), indicating that phosphate functionalization favors electrochemical stability over high intrinsic capacitance. Ni-SSBH and Ni-CNT start with the highest pre-MFC capacitances (0.96–0.97 F/g) reflecting strong faradaic CV features, but increase only modestly to 2.12–2.52 F/g during and to 3–3.4 F/g after MFC operation, incongruously that their initially aggressive redox behavior does not translate into strongly supercapacitive, biofilm-stabilized anodes over long-term cycling.

Table 1. Electrical conductivity (δ) and specific capacitance of anode electrodes in anolyte before-, during- and after MFC operation

Anode Electrode	δ ($\times 10^1$ mS/cm)	Specific capacitance (pre-MFC) F/g	Specific capacitance (during MFC) F/g	Specific capacitance (Post-MFC) F/g
Ni-RSBH	3.40 ± 0.04	0.49	8.39	51.03
Ni-PSBH	3.40 ± 0.04	0.05	6.11	3.54
Ni-SSBH	3.65 ± 0.05	0.96	2.12	3.44
Ni-CNT	2.98 ± 0.00	0.97	2.52	3.01

3.3.3 Cyclic voltammetry measurement for cathode electrodes

Unlike the anode electrodes, which were evaluated only in a laboratory-prepared anolyte, the cathode electrodes were examined in ferricyanide, KOH, and oxygenated water to clarify their performance across different catholyte environments relevant to bioelectrochemical systems. Ferricyanide and KOH represent liquid catholytes typically used in dual-chamber MFCs and MECs, whereas oxygenated water simulates the behavior of cathodes in air-cathode configurations where oxygen is the terminal electron acceptor. In ferricyanide electrolyte, Ni-RSBH, Ni-PSBH, and Ni-CNT exhibit well-defined and intense redox couples, with anodic peak currents between 0.00 and 0.0039 A within a similar potential window (Fig. 11), indicating rapid and reversible ferricyanide reduction, showing that even the less active materials can support fast electron transfer, in line with earlier ferricyanide-catholyte study [64]. Ni-SSBH shows the lowest peak currents and narrow potential range, mirroring its weaker anode performance.

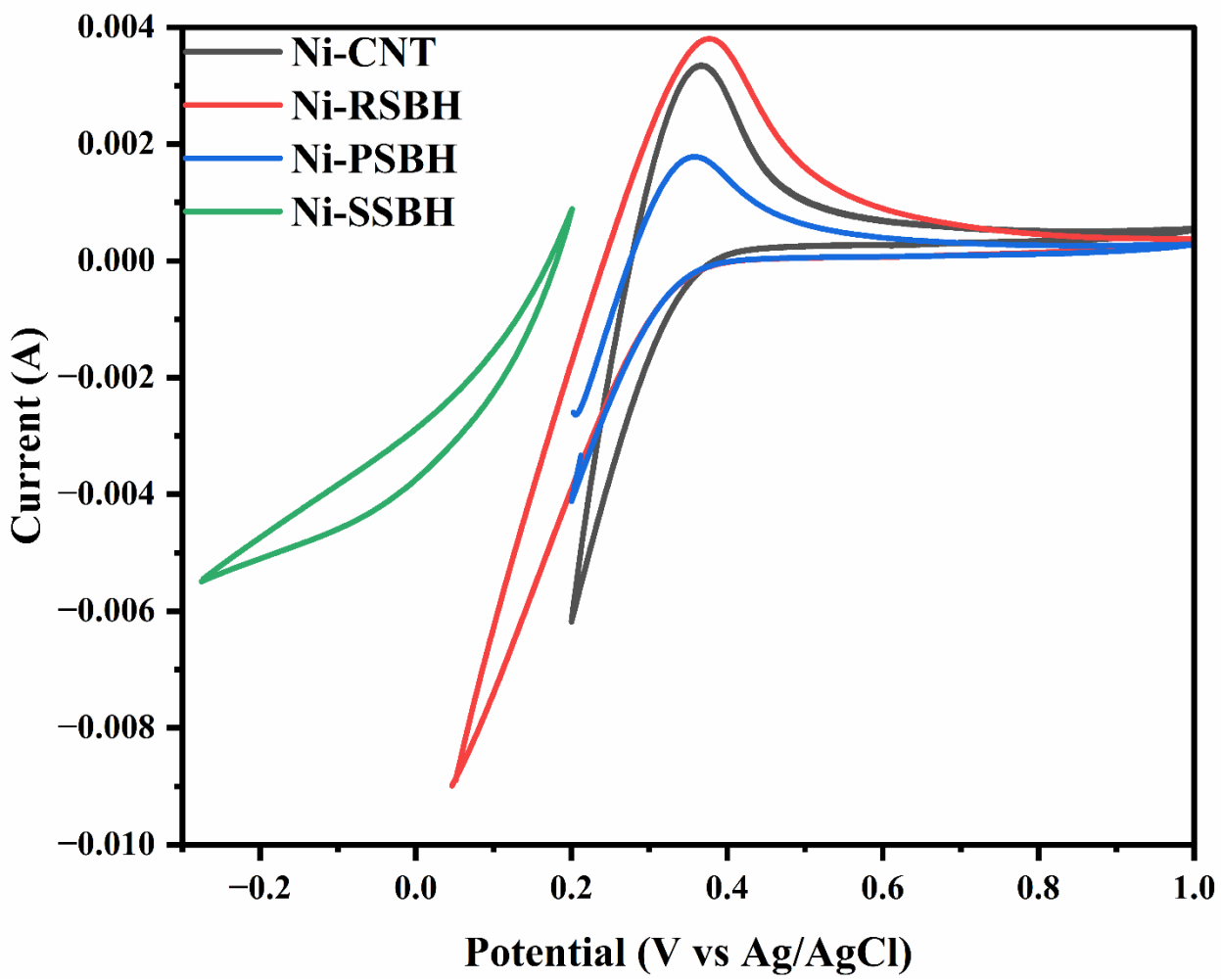

Fig. 11 CV curves of Ni-RSBH, Ni-PSBH, Ni-SSBH and Ni-CNT cathode electrodes in ferricyanide catholyte prior to MFC application

When tested in KOH, however, Ni-SSBH displays the broadest and most pronounced CV, with a large cathodic current between −0.005 and −0.019 A (Fig. 12(a)), suggesting significantly improved oxygen reduction kinetics in alkaline media compared with neutral conditions [65]. Ni-RSBH presents a single anodic peak of 0.0037 A at 0.322 V, and two cathodic peaks of 0.0026 and 0.00028 A at 0.415 and 0.197 V, respectively (Fig. *S*1), which can be ascribed to stepwise redox transitions at distinct adsorption sites within the porous hydrochar structure [66], while Ni-

PSBH follows the same pattern with lower peak currents *viz*. anodic: 0.0004 A at 0.3 V; cathodic: 0.00028 and −0.00002 A at 0.347 and 0.217 V (Fig. 12(b)). In contrast, Ni-CNT performs poorly in KOH, showing the smallest current range and lacking distinct redox peaks (Fig. 12(c)). As anticipated, oxygenated water yields the lowest currents and the slowest CV response among the three electrolytes (Fig. 12(d)), consistent with reports that ferricyanide cathodes can deliver 40–80 % higher output than dissolved-oxygen systems [67]. The overall activity order in oxygenated water is Ni-RSBH > Ni-PSBH > Ni-CNT > Ni-SSBH.

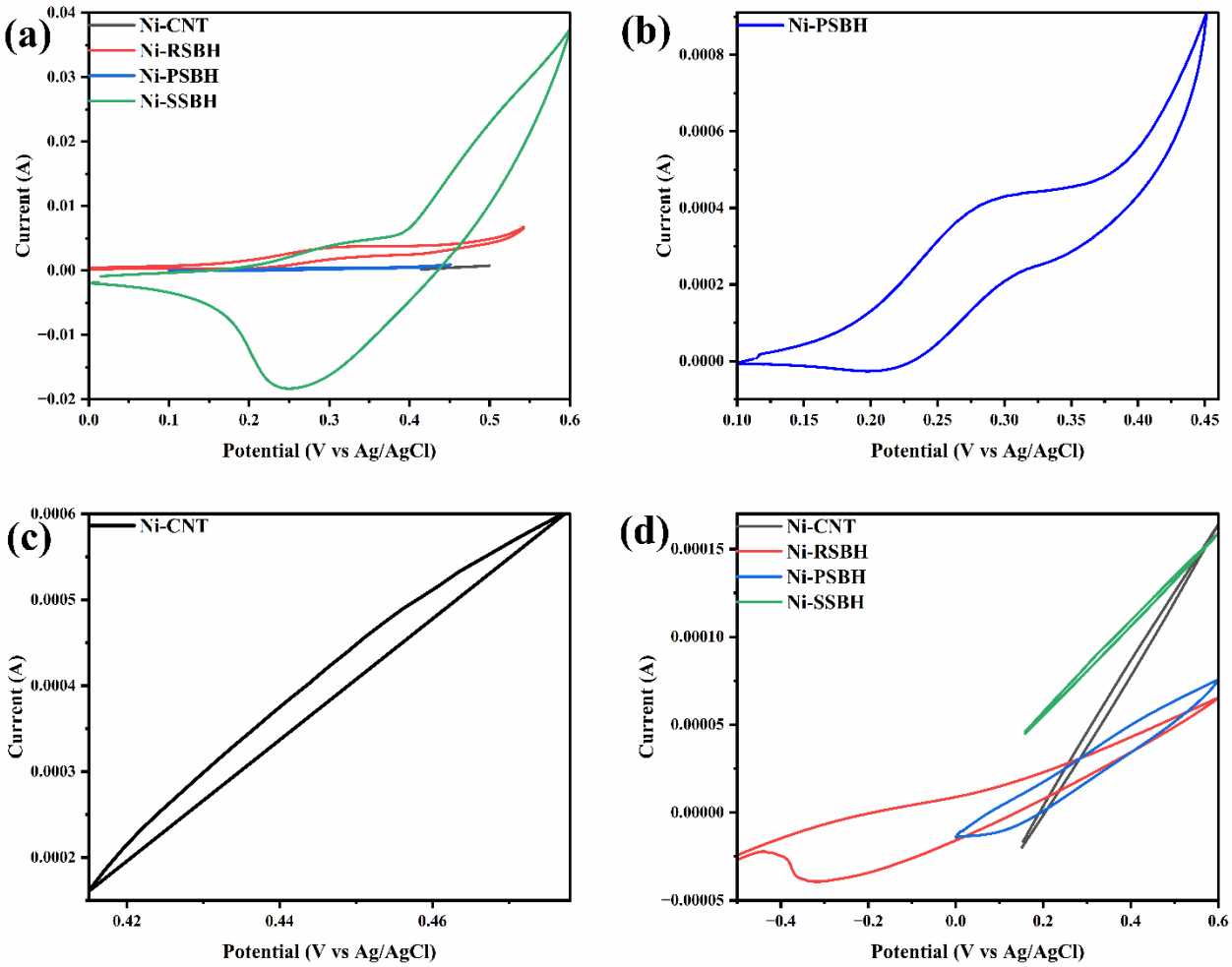

Fig. 12 CV curves of (a) Ni-RSBH, Ni-PSBH, Ni-SSBH and Ni-CNT cathode electrodes in KOH catholyte prior to MFC application, (b) Enhanced CV curve of Ni-PSBH, (c) Enhanced CV curve

of Ni-CNT, and (d) CV curves of Ni-RSBH, Ni-PSBH, Ni-SSBH and Ni-CNT cathode electrodes in oxygenated water prior to MFC application

Comparing the CV responses before- and after the MFC operation in ferricyanide, the current increased four-fold, showing multiple distinct redox peaks post-MFC (Fig. 13), unlike the single anodic peak observed pre-MFC (Fig. 11). The Ni-RSBH electrode displayed the highest currents with two anodic peaks at 0.016 A and 0.012 A, occurring at 0.50 V and 0.84 V, respectively, along with one cathodic peak of -0.009 A at 0.51 V. Ni-CNT and Ni-PSBH electrodes showed similar patterns of double anodic peaks and a single cathodic peak, but with lower current intensities compared to Ni-RSBH (Fig. 13(a)). This pattern suggests that cathodes containing RSBH, CNT, and PSBH became activated and experienced an increase in swelling ratio during MFC operation, leading to enhanced electrode performance over time [68]. These results demonstrate the electrodes' stability and durability in ferricyanide over 56 days. In contrast, the Ni-SSBH electrode exhibited a single weak cathodic peak of 0.002 A at 0.083 V (Fig. 13(b)), indicating a loss of active sites during MFC operation, and manifesting its instability in the electrolyte over time.

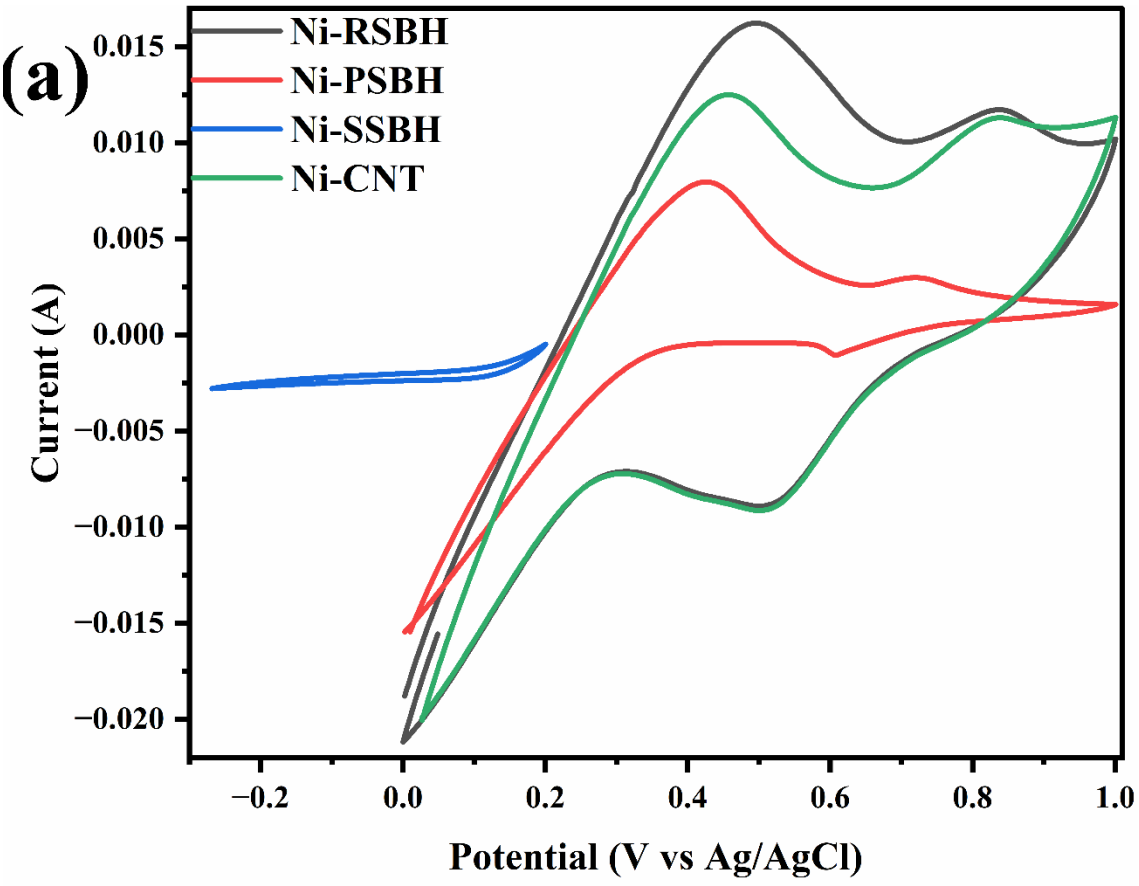
(a)
Ni-RSBH
Ni-PSBH
Ni-SSBH
Ni-CNT
Current (A)
0.015
0.010
0.005
0.000
−0.005
−0.010
−0.015
−0.020
−0.2
0.0
0.2
0.4
0.6
0.8
1.0
Potential (V vs Ag/AgCl)

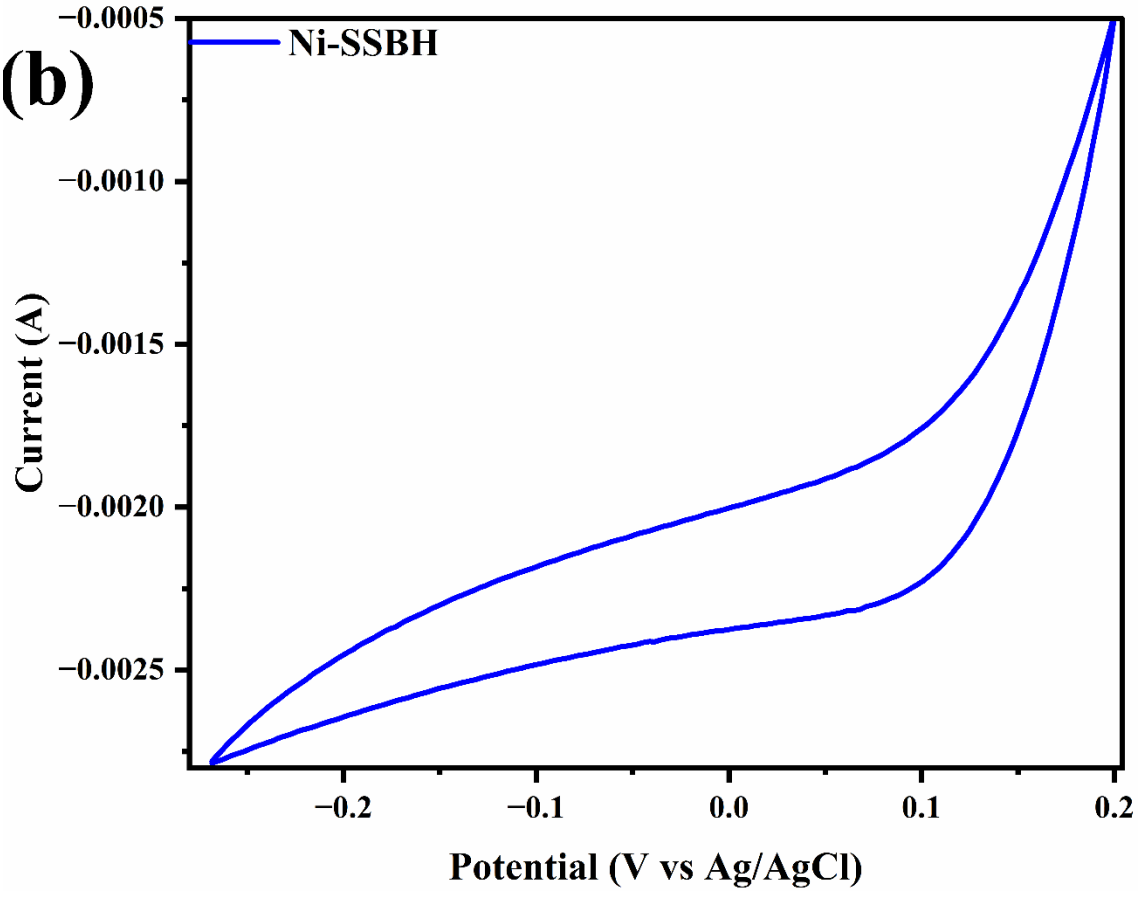
(b)
Ni-SSBH
Current (A)
−0.0005
−0.0010
−0.0015
−0.0020
−0.0025
−0.2
−0.1
0.0
0.1
0.2
Potential (V vs Ag/AgCl)

Fig. 13 (a) CV curves of Ni-RSBH, Ni-PSBH, Ni-SSBH and Ni-CNT cathode electrodes in ferricyanide post MFC application, and (b) Enhanced CV curve of Ni-SSBH electrode in ferricyanide post MFC application

The specific capacitance of cathode electrodes in ferricyanide increased markedly after MFC operation (Table 2), consistent with the enhanced CV currents and multiple redox peaks observed in Fig. 13. Ni-RSBH showed the highest capacitance rise from 9.36 to 41.44 F/g, reflecting electrode activation and swelling-induced performance improvements [69]. Ni-CNT and Ni-PSBH showed enhanced capacitance but to lesser extents compared to Ni-RSBH, while Ni-SSBH's capacitance dropped sharply, indicating active site losses and instability during MFC application as discussed earlier.

Table 2. Electrical conductivity (δ) and specific capacitance of cathode electrodes in ferricyanide, potassium hydroxide and oxygenated water before- and after MFC operation

Cathode Electrode	**δ (×10[1] mS/cm)**	**Specific capacitance in Ferricyanide (pre-MFC) F/g**	**Specific capacitance in KOH (pre-MFC) F/g**	**Specific capacitance in oxygenated water (pre-MFC) F/g**	**Specific capacitance in Ferricyanide (Post-MFC) F/g**
Ni-RSBH	3.56 ± 0.00	9.36	6.49	0.11	41.44
Ni-PSBH	4.23 ± 0.00	4.33	1.18	0.10	13.29
Ni-SSBH	4.47 ± 0.07	3.98	46.49	0.01	0.74

Ni-CNT	2.20 ± 0.04	13.45	0.05	0.07	35.75

3.3.4 Electrochemical impedance spectroscopy

When anode electrodes were utilized as the working electrode in Fig. 14, Ni-CNT exhibited the lowest overall internal resistance (R_{int}) at 81.93 Ω, primarily driven by its minimal charge transfer resistance (R_{ct}) at 2.22 Ω and electrolyte resistance (R_{el}) at 78.60 Ω (Fig. 14(d) and Fig. *S*2). Ni-PSBH showed R_{int} of 194.93 Ω (R_{ct}: 4.04 Ω, R_{el}: 79.81 Ω, Fig. 14(b) and Fig. *S*2), outperforming Ni-SSBH (124.02 Ω R_{int}, R_{ct}: 49.96 Ω) and Ni-RSBH (1565.42 Ω R_{int}, R_{ct}: 1434.1 Ω). Although, the highly purified, expensive and industrial-grade CNT recorded the superior resistance as anode modifier, PSBH demonstrate a notable breakthrough by reducing the R_{ct} by over 95 % compared to RSBH, attributed to introduced phosphate groups that boost hydrophilicity, active sites, and electroactive biofilm formation. These notable traits are principal for sustainable, low-cost biomass electrodes versus expensive CNT.

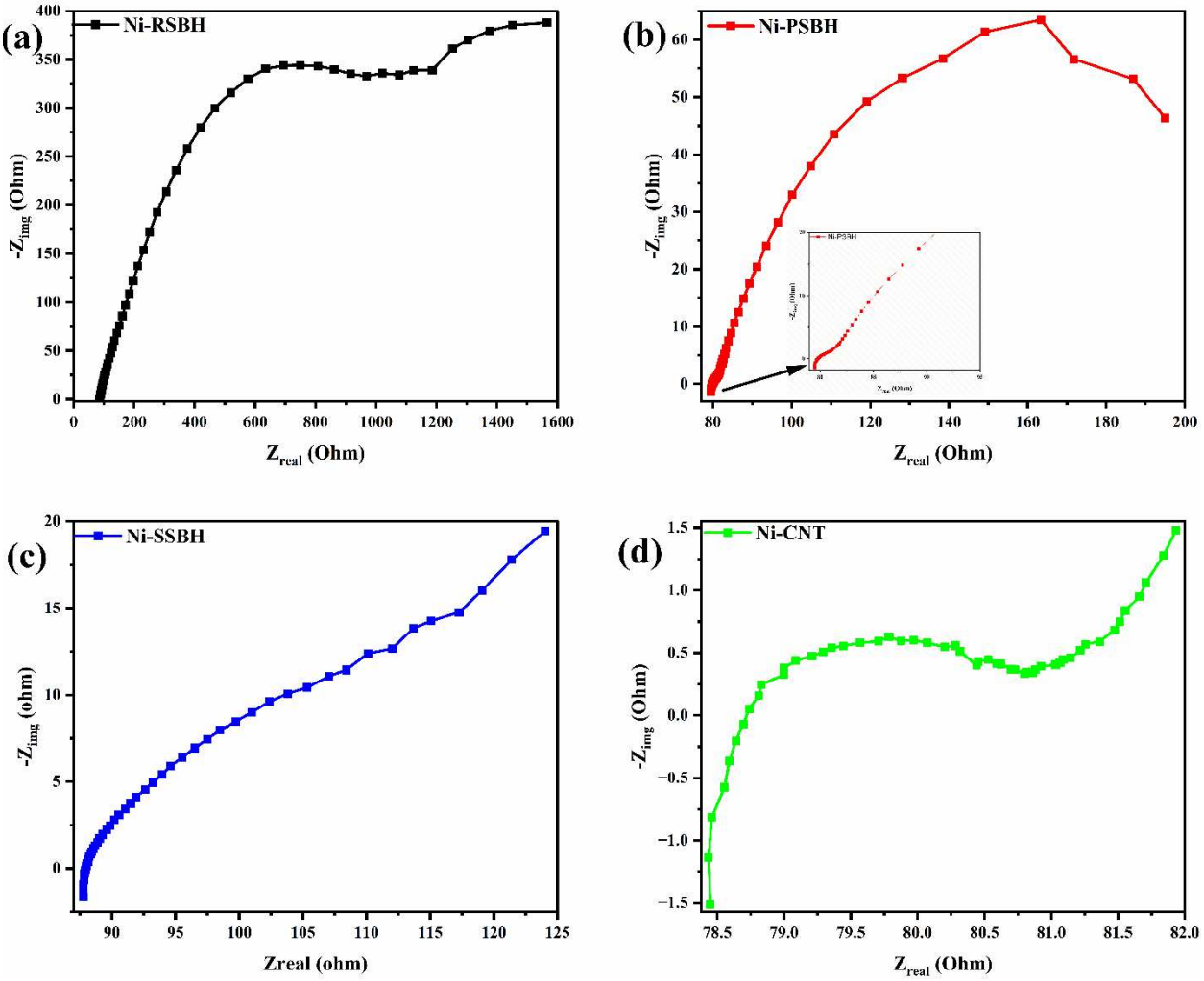

Fig. 14 Nyquist plot of (a) Ni-RSBH, (b) Ni-PSBH, (c) Ni-SSBH and (d) Ni-CNT with anode as working electrode during MFC operation

Conversely, for the cathode electrode in Fig. 15, Ni-CNT displayed the highest R_{int} at 12729.21 Ω, dominated by an exceptionally high R_{ct} of 13575 Ω despite low R_{el} (64.83 Ω), indicating sluggish oxygen reduction reaction (ORR) kinetics and poor catalytic activity (Fig. 15 (d) and Fig. *S*3). Ni-PSBH achieved the lowest R_{int} at 1076.86 Ω (R_{ct}: 1072.8 Ω, R_{el}: 168.21 Ω), followed by Ni-RSBH (1677.46 Ω R_{int}, R_{ct}: 1170.3 Ω) and Ni-SSBH (2035.69 Ω R_{int}, R_{ct}: 2024.6 Ω). This reversal in performance underscores the novelty and superiority of Ni-RSBH, Ni-PSBH, and Ni-SSBH over

Ni-CNT at the cathode, where raw char and its chemical modification variants enhance ORR *via* heteroatom doping, increased porosity, and pseudocapacitive effects from higher constant phase element value (Ni-PSBH: 135 μMho*s$^{\wedge}$N *vs.* Ni-CNT: 13 μMho*s$^{\wedge}$N), reducing R_{ct} by up to 92 % relative to Ni-CNT (Fig. 15 and Fig. *S*3).

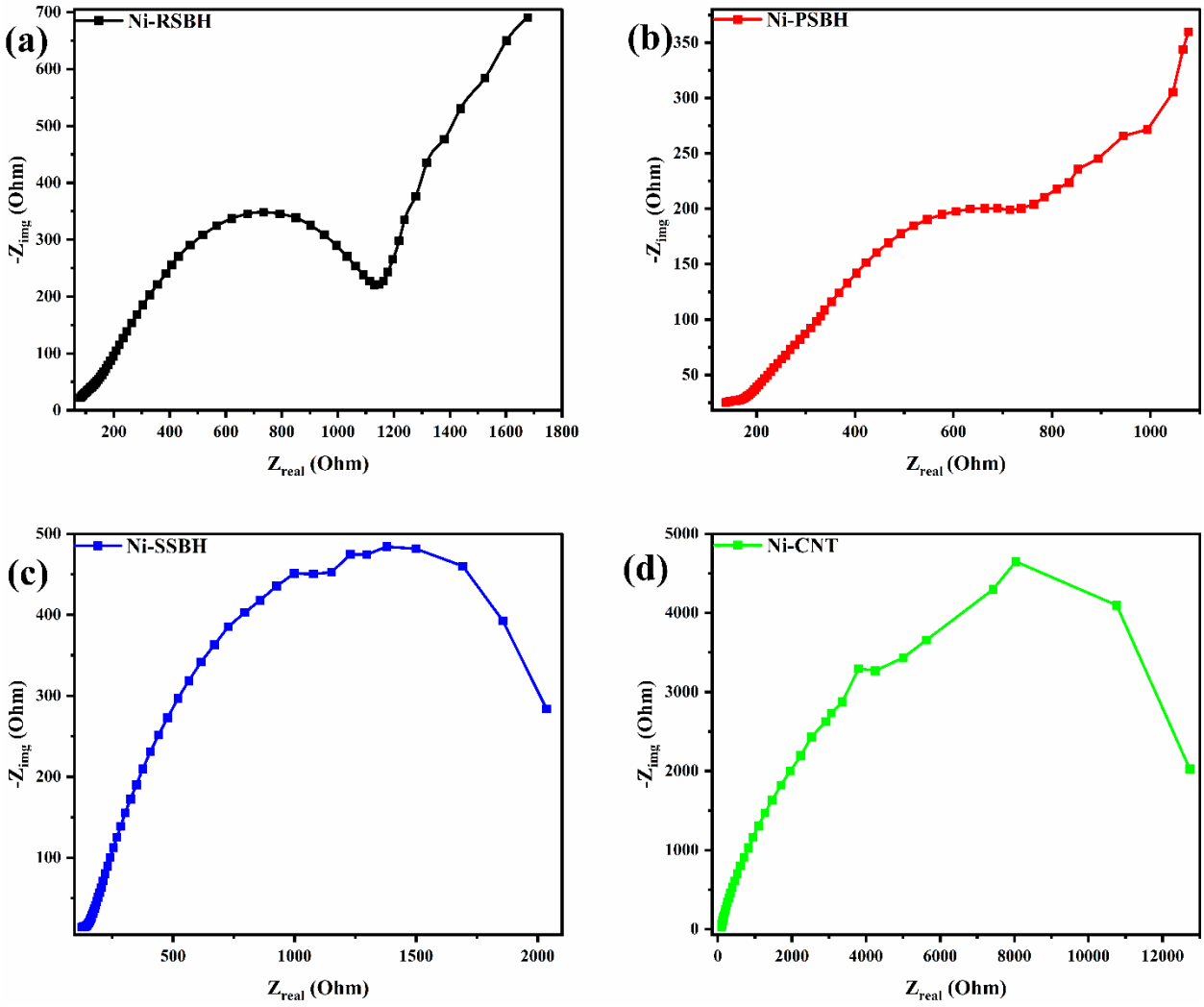

Fig. 15 Nyquist plot of (a) Ni-RSBH, (b) Ni-PSBH, (c) Ni-SSBH and (d) Ni-CNT with cathode as working electrode during MFC operation

4. Conclusion

Sugarcane bagasse–derived hydrochars demonstrated that low-cost, waste-based carbons can rival and even surpass engineered nanomaterials as electrodes in microbial fuel cells. Drawing on a single, abundant agro-residue, this work shows that raw hydrochar (Ni-RSBH) delivered the highest peak power density (1008 mW/m²) and the largest post-operation anode capacitance (51.03 F/g), outperforming commercial carbon nanotube electrodes under identical operating conditions. Phosphated hydrochar (Ni-PSBH) provided the most stable voltage output over 56 days of continuous operation, while sulfonated hydrochar (Ni-SSBH) highlighted the performance penalties of over-acidification at the biofilm–electrode interface, underscoring the importance of balancing conductivity, surface chemistry, and microbial compatibility.

By integrating structural, thermal, electrochemical, and long-term biofilm analyses, the study clarifies how specific functional groups and microstructures govern charge transfer, capacitance evolution, and biofilm development on hydrochar electrodes. The finding that minimally processed, hydrothermally produced RSBH can outperform a high-purity CNT benchmark directly supports the replacement of expensive nanocarbons with scalable, circular-economy materials in bioelectrochemical systems. Collectively, these results position sugarcane bagasse hydrochar as a technically competitive and economically attractive electrode platform, opening a practical route toward cost-effective, deployable microbial fuel cells for coupled wastewater treatment and distributed renewable power generation.

Conflict of Interest

The authors declare no conflicts of interest that could influence the objectivity of this research.

Acknowledgement

The authors gratefully acknowledge the AAIBE Chair for Renewable Energy Grant (202407KETTHA) from Universiti Tenaga Nasional, Malaysia, as well as the research facilities and support provided by Universiti Malaya, Malaysia.

Funding

AAIBE Chair for Renewable Energy (Grant number: 202407KETTHA), Universiti Tenaga Nasional, Malaysia.

References

1. Abibu WA, Karapinar I, Yunusa UM, Sirajudeen AAO, Ibrahim S. Effects of divalent cations and electron mediators on acetone–butanol–ethanol (ABE) fermentation of Ficus carica. Biofuels. 2025:1-20. doi: 10.1080/17597269.2025.2551381.

2. Abibu WA, Karapinar I, Yunusa UM, Sirajudeen AAO, Ibrahim S, Sakariyau AO, et al. Effect of Substrate Concentration on Simultaneous Acetone-Butanol-Ethanol Fermentation and Biohydrogen Production from Fig (Ficus carica). JREE. 2025;12(4):1-8. doi: 10.30501/jree.2025.511732.2303.

3. Desing H, Schlesier H, Gauch M. Solar basic service—an idea for just acceleration of the energy transition. PRGE. 2025;7(2):023002. doi: 10.1088/2516-1083/adc370.

4. Forster PM, Smith C, Walsh T, Lamb WF, Lamboll R, Cassou C, et al. Indicators of Global Climate Change 2024: annual update of key indicators of the state of the climate system and human influence. Earth Syst Sci Data. 2025;17(6):2641-80. doi: 10.5194/essd-17-2641-2025.

5. Sirajudeen AO, Ibrahim S, Adediji AS, Hussein MY, Abibu WA. Isolation of Exoelectrogenic Bacteria from Palm Oil Mill Effluent and Their Application in Microbial Fuel Cell. Nigerian Journal of Biotechnology. 2024;41(1):110-20. doi: 10.4314/njb.v41i1.12.

6. Olayiwola Sirajudeen AA, Mohamad Annuar MS, Ishak KA, Yusuf H, Subramaniam R. Innovative application of biopolymer composite as proton exchange membrane in microbial fuel cell utilizing real wastewater for electricity generation. J Clean Prod. 2021;278:123449. doi: 10.1016/j.jclepro.2020.123449.

7. Sirajudeen AAO, M. Annuar MS. Polymeric nanocomposition for innovative functional enhancement of electrodes and proton exchange membrane in microbial fuel cell. J Serb Chem Soc. 2021;86(1):1-23. doi: 10.2298/JSC200402054S.

8. Sirajudeen AO, Annuar MSM, Ibrahim S. Enhanced microbial fuel cell performance using carbon nanotube-composited medium-chain-length polyhydroxyalkanoates-co-polycaprolactone blends as anode coatings. Chem Eng Commun. 2025;212(9):1382-94. doi: 10.1080/00986445.2025.2466837.

9. Srivastava S, Gupta AK, Gupta P. Harnessing Microbial Fuel Cells for Drug Degradation: Role of Microorganisms and Innovations in Anode and Cathode Materials. J Water Proc Eng. 2025;74:107881. doi: 10.1016/j.jwpe.2025.107881.

10. Sirajudeen AAO, Annuar MSM, Subramaniam R. Composite of medium-chain-length polyhydroxyalkanoates-co-methyl acrylate and carbon nanotubes as innovative electrodes modifier in microbial fuel cell. Biotechnology and Applied Biochemistry. 2021;68(2):307-18. doi: 10.1002/bab.1928.

11. Yeo RYZ, Ang WL, Bakar MHA, Ismail M, Salehmin MNI, Yu EH, et al. Multi-Array Tubular Microbial Fuel Cell-Based Biosensor with Membrane Electrode Assembled Air-Cathodes. Fuel Cells. 2025;25(1):e202400035. doi: 10.1002/fuce.202400035.

12. Zheng Q, Ma Z, Qiu Y, Zhang Z, Wang R, Liu S. Boosting microbial fuel cell performance with Co-Nx doped carbon nanotubes/graphene biomimetic anode composites. Appl Surf Sci. 2025;699:163163. doi: 10.1016/j.apsusc.2025.163163.

13. Pan Q-R, Ouyang Y-Q, Jiang H-H, Ou D-N, Zhong J-Y, Li N. Bifunctional electrode materials: Enhancing microbial fuel cell efficiency with 3D hierarchical porous Fe3O4/Fe-N-C structures. Bioelectrochemistry. 2025;161:108829. doi: 10.1016/j.bioelechem.2024.108829.

14. Zhang C, Zeng X, Xu X, Nie W, Dubey BK, Ding W. PDA-Fe3O4 decorated carbon felt anode enhancing electrochemical performance of microbial fuel cells: Effect of electrode materials on electroactive biofilm. Chemosphere. 2024;355:141764. doi: 10.1016/j.chemosphere.2024.141764.

15. Ahmad A. Exploitation of moringa biomass to fabricate graphene electrode for electricity generation with wastewater treatment through microbial fuel cells. Biomass Convers Biorefin. 2025;15(9):13469-83. doi: 10.1007/s13399-024-06134-8.

16. He X, Ma S, Ma P, Cao R, Tian X, Lu Y, et al. Waste biomass durian shell carbon to derive N-rich porous microbial fuel cell anode for simultaneous dye degradation and electricity generation. Bioresour Technol. 2025;436:132984. doi: 10.1016/j.biortech.2025.132984.

17. Ouyang B, Zhang Z, Chen F, Li F, Fu M-L, Lan H, et al. Energy production and denitrogenation performance by sludge biochar based constructed wetlands-microbial fuel cells

system: Overcoming carbon constraints in water. Water Res. 2025;273:123024. doi: 10.1016/j.watres.2024.123024.

18. Goglio A, Carrara A, Elboghdady HGE, Cucina M, Clagnan E, Soggia G, et al. The performance of biochar waste-derived electrodes in different bio-electrochemical applications. J Power Sources. 2025;625:235623. doi: 10.1016/j.jpowsour.2024.235623.

19. Deivayanai VC, Thamarai P, Kamalesh R, Shaji A, Yaashikaa PR, Saravanan A. A sustainable approach on utilization of waste-derived biochar in microbial fuel cell toward net-zero coalition. Nano-Struct Nano-Objects. 2024;39:101307. doi: 10.1016/j.nanoso.2024.101307.

20. Rodríguez-Narvaez OM, Medina-Orendain DA, Mendez-Alvarado LN. Chapter 14 - Functionalized green carbon-based nanomaterial for environmental application. In: Koduru JR, Karri RR, Mubarak NM, Bandala ER, editors. Sustainable Nanotechnology for Environmental Remediation. Elsevier; 2022. p. 347-82.

21. Prasannamedha G, Kumar PS, Balasubramani SR, Parthasarathy V, Deehen AD, Jananie E, et al. Engineering properties of hydrochar fabricated from hydrothermal carbonization of lignocellulosic biomass: Practice as adsorbent and catalyst in water treatment. J Water Proc Eng. 2025;74:107739. doi: 10.1016/j.jwpe.2025.107739.

22. Sun J, Benavente V, Jansson S, Mašek O. Comparative characterisation and phytotoxicity assessment of biochar and hydrochar derived from municipal wastewater microalgae biomass. Bioresour Technol. 2023;386:129567. doi: 10.1016/j.biortech.2023.129567.

23. Islam MT, Sultana AI, Chambers C, Saha S, Saha N, Kirtania K, et al. Recent Progress on Emerging Applications of Hydrochar. Energies. 2022;15(24):9340. doi: 10.3390/en15249340.

24. Tahir H, Saad M, Shafi N, Muslim F. Chapter 3 - Composite. In: Ghaedi M, editor. Interface Science and Technology. Elsevier; 2021. p. 211-78.

25. Melesse GT, Hone FG, Mekonnen MA. Extraction of Cellulose from Sugarcane Bagasse Optimization and Characterization. Adv mater sci eng. 2022;2022(1):1712207. doi: 10.1155/2022/1712207.

26. Ajala EO, Ighalo JO, Ajala MA, Adeniyi AG, Ayanshola AM. Sugarcane bagasse: a biomass sufficiently applied for improving global energy, environment and economic sustainability. Bioresour Bioprocess. 2021;8(1):87. doi: 10.1186/s40643-021-00440-z.

27. Basha DB, Ahmed S, Ahmed A, Gondal MA. Recent advances on nitrogen doped porous carbon micro-supercapacitors: New directions for wearable electronics. J Energy Storage. 2023;60:106581. doi: 10.1016/j.est.2022.106581.

28. Saad Agwa I, Zeyad AM, Tayeh BA, Adesina A, de Azevedo ARG, Amin M, et al. A comprehensive review on the use of sugarcane bagasse ash as a supplementary cementitious material to produce eco-friendly concretes. Mater Today Proc. 2022;65:688-96. doi: 10.1016/j.matpr.2022.03.264.

29. Li Y, Meas A, Shan S, Yang R, Gai X. Production and optimization of bamboo hydrochars for adsorption of Congo red and 2-naphthol. Bioresour Technol. 2016;207:379-86. doi: 10.1016/j.biortech.2016.02.012.

30. Katibi KK, Azis RS, Shitu IG, Ismail I, Kien CS, Pah LK, et al. Tuning synthesis temperature spectrum to unlock multifunctional potential in multi-walled carbon nanotubes for EMI shielding and optical applications. J Ind Eng Chem. 2025;146:826-52. doi: 10.1016/j.jiec.2025.02.034.

31. Katibi KK, Md Yunos KF, Man HC, Aris AZ, Nor MZM, Azis RS. Influence of Functionalized Hematite Nanoparticles as a Reinforcer for Composite PVDF-PEG Membrane for BPF Rejection: Permeability and Anti-fouling Studies. Journal of Polymers and the Environment. 2023;31(2):768-90. doi: 10.1007/s10924-022-02605-z.

32. Murugaiyan S, Shabanur Matada MS, Kuppuswamy GP, Velappa Jayaraman S, Di Natale C, Sivalingam Y. Carbon Electrodes Coated with TiO2–Cu-MOF Composites for Nonenzymatic Detection of Ascorbic Acid. ACS Appl Nano Mater. 2025;8(42):20164-76. doi: 10.1021/acsanm.5c02223.

33. Park I-S, Li W, Manthiram A. Fabrication of catalyst-coated membrane-electrode assemblies by doctor blade method and their performance in fuel cells. J Power Sources. 2010;195(20):7078-82. doi: 10.1016/j.jpowsour.2010.05.004.

34. Sirajudeen AAO, Sanusi JF, Apantaku JT, Ibrahim S, Mohamad Annuar MS. Application of Novel Bacillus spp. Isolated from Palm Oil Mill Effluent in Microbial Fuel Cell for Electricity Generation and Wastewater Treatment. IOP Conference Series: Earth and Environmental Science. 2025;1560(1):012014. doi: 10.1088/1755-1315/1560/1/012014.

35. Logan BE. Microbial fuel cells. John Wiley & Sons; 2008.

36. Yusuf H, Annuar MSM, Syed Mohamed SMD, Subramaniam R. Medium-chain-length poly-3-hydroxyalkanoates-carbon nanotubes composite as proton exchange membrane in microbial fuel cell. Chem Eng Commun. 2019;206(6):731-45. doi: 10.1080/00986445.2018.1521392.

37. Phachaipum S, Prapainainar C, Prapainainar P. Proton-exchange polymer composite membrane of Nafion and microcrystalline cellulose for performance improvement of direct glycerol fuel cell. Int J Hydrogen Energy. 2024;52:1111-20. doi: 10.1016/j.ijhydene.2023.10.091.

38. Adeleke AO, Dar MA, Dele-Afolabi TT, Omar RC, Roslan R, Ahmad A, et al. Callerya Atropurpurea shells derived nitrogen doped carbon quantum dots of electrodes for symmetrical and asymmetrical supercapacitors. Sci Rep. 2025;15(1):30209. doi: 10.1038/s41598-025-15098-2.

39. Dar MA, Majid SR, Sarkar S, Kalpana S, Arularasan P, Rather AA, et al. Synthesis and characterization of binder-free Ni, Cu, Mn, and Co metal–organic frameworks for supercapacitors. Ionics. 2025;31(4):3715-26. doi: 10.1007/s11581-025-06138-y.

40. Aliyu M, Abdullah AH, Tahir MIbM. Adsorption tetracycline from aqueous solution using a novel polymeric adsorbent derived from the rubber waste. J Taiwan Inst Chem Eng. 2022;136:104333. doi: 10.1016/j.jtice.2022.104333.

41. Anitha S, Vaideki K. ATR-FTIR Analysis on Aliphatic Hydrocarbon Bond (C-H) Formation and Carboxyl Content during the Ageing of DC Air Plasma Treated Cotton Cellulose and Its Impact on Hydrophilicity. OPMR. 2022;4(1):12-23. doi: 10.30564/opmr.v4i1.4610.

42. Aliyu M, Rashid U, Tsubota T, Wan Ab Karim Ghani WA, Mohd Salleh MA, Khuong DA, et al. A novel magnetic bifunctional hydrochar catalyst derived from palm leaf residue for biodiesel production: kinetic and thermodynamic studies. J Chem Technol Biotechnol. 2025;100(3):530-44. doi: 10.1002/jctb.7792.

43. Qi Y, Wei D, Shi G-M, Zhang M, Qi Y. Amorphous/Nanocrystalline Carbonized Hydrochars with Isomeric Heterogeneous Interfacial Polarizations for High-performance Microwave Absorption. Sci Rep. 2019;9(1):12429. doi: 10.1038/s41598-019-48926-3.

44. Aliyu M, Rashid U, Ghani WAWAK, Salleh MAM, Hazmi B, Alharthi FA, et al. Waste Palm Leaves-Based Hydrochar Support Catalytic Esterification of Palm Fatty Acid Distillate. Bioenergy Res. 2024;17(4):2413-28. doi: 10.1007/s12155-024-10789-6.

45. Chhabra T, Dwivedi P, Krishnan V. Acid functionalized hydrochar as heterogeneous catalysts for solventless synthesis of biofuel precursors. Green Chem. 2022;24(2):898-910. doi: 10.1039/D1GC03330A.

46. Xu Z, Ma X, Liao J, Osman SM, Wu S, Luque R. Effects on the Physicochemical Properties of Hydrochar Originating from Deep Eutectic Solvent (Urea and ZnCl2)-Assisted Hydrothermal Carbonization of Sewage Sludge. ACS Sustain Chem Eng. 2022;10(13):4258-68. doi: 10.1021/acssuschemeng.2c00086.

47. Chang J, Yu S, Liao Y, Guan X, Gao H, Li Y. One-Step Pyrolysis Fabrication of Magnetic Bagasse Biochar Composites with Excellent Lead Adsorption Performance. ACS Omega. 2022;7(47):42854-64. doi: 10.1021/acsomega.2c04882.

48. Praipipat P, Ngamsurach P, Sanghuayprai A. Modification of sugarcane bagasse with iron(III) oxide-hydroxide to improve its adsorption property for removing lead(II) ions. Sci Rep. 2023;13(1):1467. doi: 10.1038/s41598-023-28654-5.

49. Shanavas Laila L, M.Sambasivam K. Enhancing the efficiency of mortar mixes by rice husk hydrochar using response surface methodology: An experimental study for property improvement

and sustainable construction applications. RINENG. 2025;27:106019. doi: 10.1016/j.rineng.2025.106019.

50. Zhou F, Li K, Hang F, Zhang Z, Chen P, Wei L, et al. Efficient removal of methylene blue by activated hydrochar prepared by hydrothermal carbonization and NaOH activation of sugarcane bagasse and phosphoric acid. RSC Adv. 2022;12(3):1885-96. doi: 10.1039/D1RA08325B.

51. Hassa W, Fiala K, Apiraksakorn J, Leesing R. Sugarcane bagasse valorization through integrated process for single cell oil, sulfonated carbon-based catalyst and biodiesel co-production. Carbon Resour Convers. 2025;8(2):100245. doi: 10.1016/j.crcon.2024.100245.

52. Zhou N, Chen H, Feng Q, Yao D, Chen H, Wang H, et al. Effect of phosphoric acid on the surface properties and Pb(II) adsorption mechanisms of hydrochars prepared from fresh banana peels. J Clean Prod. 2017;165:221-30. doi: 10.1016/j.jclepro.2017.07.111.

53. Guanfeng L, WU KK, Huang B. Effects of Small Amounts of Phosphoric Acid as Additive in the Preparation of Microporous Activated Carbons. Mater Sci. 2018;24(4):362-6. doi: 10.5755/j01.ms.24.4.18999

54. Li F, Zimmerman AR, Zheng Y, Yang Y, Huang J, Zhang Y, et al. P-enriched hydrochar for soil remediation: Synthesis, characterization, and lead stabilization. Sci Total Environ. 2021;783:146983. doi: 10.1016/j.scitotenv.2021.146983.

55. Malool ME, Keshavarz Moraveji M, Shayegan J. Optimized production, Pb(II) adsorption and characterization of alkali modified hydrochar from sugarcane bagasse. Sci Rep. 2021;11(1):22328. doi: 10.1038/s41598-021-01825-y.

56. Veer Raghavulu S, Venkata Mohan S, Venkateswar Reddy M, Mohanakrishna G, Sarma PN. Behavior of single chambered mediatorless microbial fuel cell (MFC) at acidophilic, neutral and alkaline microenvironments during chemical wastewater treatment. Int J Hydrogen Energy. 2009;34(17):7547-54. doi: 10.1016/j.ijhydene.2009.05.071.

57. Yuan H, Hou Y, Abu-Reesh IM, Chen J, He Z. Oxygen reduction reaction catalysts used in microbial fuel cells for energy-efficient wastewater treatment: a review. Mater Horiz. 2016;3(5):382-401. doi: 10.1039/C6MH00093B.

58. Rismani-Yazdi H, Carver SM, Christy AD, Tuovinen OH. Cathodic limitations in microbial fuel cells: An overview. J Power Sources. 2008;180(2):683-94. doi: 10.1016/j.jpowsour.2008.02.074.

59. Yang Y, Liu C, Su M, Jin K, Li L, Tian H, et al. Kinetic Mechanism and Structural Design of Thick Electrodes in Lithium-Ion Batteries: Challenges and Optimization Strategies. Small. 2025;21(43):e06931. doi: 10.1002/smll.202506931.

60. Yang Q, Luo D, Liu X, Guo T, Zhao X, Zheng X, et al. Improving the anode performance of microbial fuel cell with carbon nanotubes supported cobalt phosphate catalyst. Bioelectrochemistry. 2021;142:107941. doi: 10.1016/j.bioelechem.2021.107941.

61. Ramírez-Soria EH, García-Dalí S, Munuera JM, Carrasco DF, Villar-Rodil S, Tascón JMD, et al. A Simple and Expeditious Route to Phosphate-Functionalized, Water-Processable Graphene for Capacitive Energy Storage. ACS Appl Mater Interfaces. 2021;13(46):54860-73. doi: 10.1021/acsami.1c12135.

62. Li H, Meng R, Guo Y, Chen B, Jiao Y, Ye C, et al. Reversible electrochemical oxidation of sulfur in ionic liquid for high-voltage Al-S batteries. Nat Commun. 2021;12(1):5714. doi: 10.1038/s41467-021-26056-7.

63. Wang Y, Yu M, Wang Y, Ma Z, Qiu Y, Lv C, et al. Electrochemically activated carbon nanotube anodes for enhanced microbial fuel cell performance. Next Energy. 2025;8:100255. doi: 10.1016/j.nxener.2025.100255.

64. Cao Y, Xu S, Tian Y, Lan F, Zhang X, Liu Y, et al. Enhancing the oxygen reduction reaction in microbial fuel cell by using NiFe-LDH@NiCo2S4@MWCNT as cathode catalyst. Int J Hydrogen Energy. 2025;103:589-96. doi: 10.1016/j.ijhydene.2025.01.235.

65. Wei L, Han H, Shen J. Effects of cathodic electron acceptors and potassium ferricyanide concentrations on the performance of microbial fuel cell. Int J Hydrogen Energy. 2012;37(17):12980-6. doi: 10.1016/j.ijhydene.2012.05.068.

66. Trafela Š, Zavašnik J, Šturm S, Rožman KŽ. Formation of a Ni(OH)2/NiOOH active redox couple on nickel nanowires for formaldehyde detection in alkaline media. Electrochimica Acta. 2019;309:346-53. doi: 10.1016/j.electacta.2019.04.060.

67. Elangovan K, Saravanan P, Campos CH, Sanhueza-Gómez F, Khan MMR, Chin SY, et al. Outline of microbial fuel cells technology and their significant developments, challenges, and prospects of oxygen reduction electrocatalysts. Front Chem Eng. 2023;Volume 5 - 2023. doi: 10.3389/fceng.2023.1228510.

68. Tan S, Wang R, Dong J, Zhang K, Zhao Z, Yin Q, et al. Hydrothermal-mediated in-situ nitrogen doping to prepare biochar for enhancing oxygen reduction reactions in microbial fuel cells. Bioresour Technol. 2025;416:131789. doi: 10.1016/j.biortech.2024.131789.

69. Schonvogel D, Nowotny M, Worieschеck T, Multhaupt H, Wagner P, Dyck A, et al. Hydrothermal Carbonization-Derived Carbon from Waste Biomass as Renewable Pt Support for Fuel Cell Applications: Role of Carbon Activation. Energy Technol. 2019;7(11):1900344. doi: 10.1002/ente.201900344.

Supplementary Files

This is a list of supplementary files associated with this preprint. Click to download.

- Supplementarymaterial.docx